

Laura Fields
Paul Lebrun
Seongtae Park
Amit Bashyal
Blake Watson
January 28, 2014

LBNE Beam Alignment Tolerances and Systematic Uncertainties

This note describes a study of beam alignment tolerances and systematic uncertainties that was conducted in the winter of 2013-2014. For each beam alignment parameter listed in Table 1, we evaluate the systematic uncertainty on the unoscillated muon neutrino flux assuming the nominal tolerances listed in Table 1. In addition to providing a preliminary estimate of uncertainties that can be input to physics studies, this work also provides valuable input to the beamline group that will inform the design of hadron monitors and other beam alignment tools. The note is organized as follows: Section 1 describes the simulation used to execute the study, the procedure for extracting systematic uncertainties is reviewed in Section 2, the results are summarized in Section ???. Plots showing the neutrino flux in various beam configurations and the fits used to extract systematic uncertainties are available in Appendices ???- ???

Target position (each end)	0.5 mm
Horn 1 position (each end)	0.5 mm
Horn 2 position (each end)	0.5 mm
Far detector position	21 m
Decay pipe position	20 mm
Decay pipe radius	0.1 m
Horn current	2 kA
Horn water layer thickness	0.5 mm
Beam size at target	0.1 mm
Misalignment of shielding blocks	1 cm
Baffle scraping	0.25%
Beam position at target	0.45 mm
Beam angle at target	70 μ rad
Near detector position	255 mm
Horn conductor skin depth	6 mm
Target density	2%

Table 1: Sources of beam misalignment and their expected tolerances, which were obtained from the LBNE CDR [?] where applicable and from conversations with beam experts otherwise.

1 Description of Beam Simulation

This section describes the motivation, goals and scope of the Geant4 [?] application used in the determination of systematics effects for the LBNE beam line. As the application, named g4lbne-v3, is to a large extent self-describing, this is not a “user’s manual”, rather a memo on some technical aspects of the software. We start by stating the design requirements gathered after producing results with the previous of the software, present our adopted solution to fix limitations of g4lbne-v2 and comment on some architectural features of the code.

1.1 Requirements for g4lbne-v3

These requirements were gathered informally during our weekly meeting, over a period of a few weeks, back in April through June 2013. They were:

1. Support the studies of alignments tolerances, particularly for the Horns and the targets. While the previous version, g4lbne-v2 allowed the users to change the coordinates of sections of the horns, results were found to be difficult to understand without the confidence that the Geant4 geometry was sound. That is, that both the volumes were set as intended by the user, and the Geant4 tracking was self consistent, with no volume overlap, or other limitations that were hard to debug. While details of the geometry was set by the ASCII geometry data file, the overall program flow was determined by the

Geant4 User Interface (G4UI) data cards, causing occasional confusion.

2. Back then, the first phase of LBNE consistent of using the NUMI beamline design, the so-called 700 kW option, including it's horns and target. Detailed engineering drawing were therefore available, allowing us to implement an actual and precise geometry in our simulation. Such a drive for correctness makes sense in the context of the study of systematic effects.
3. Allow for some optimization of the geometry, to enhance the neutrino flux around both the first and second oscillation peaks, while mitigating the high energy component of the neutrino flux, while preserving the level of details required for correctness. Such an optimization is achieved through changing the geometrical configuration of the target, horns and decay pipe length and radius.
4. Upgrade the existing code to Geant4 v4.9.6. While most of the results were obtained with v4.9.3.p04, the code ought to run with the current release of the Geant4 tool kit, for further ease of maintenance (forward compatibility).

1.2 Design approach

The relatively short ASCII file that described the geometry in `g4lbne-v2` seemed convenient. However, it's design and usage does not fully support a formal data specification language, leading to possible confusion. Also, it's concept and implementation predates the introduction of the Geant4, in particular, it's User Interface. This "Geant4" standard allows for a tighter control of what can or can not be changed at a given phase of the execution of the code. The "data cards", distinct set of run-time instructions can be documented, inline, in the code via the `setGuidance` method. While more restrictive than a free-form ASCII file, it seemed safer, and we opted to completely remove the ASCII input file. In addition, the `g4lbne` specific G4UI data cards are meant to express "controlled change" on a baseline design. This means that the "baseline" configuration parameters is hard coded. Changes to it are considered bug fixes, and are tracked through the code management system. This approach is possible, as the NUMI configuration is well established. However, for both systematic studies and optimization, changes are necessary, but were agreed upon at the onset, and, for each of the studies, specific data cards have been introduced. While both using and maintaining the `g4lbne-v3` application, it seemed essential to clearly distinguish between a change in the geometry due to an optimization and those due to the simulation of unavoidable mis-alignment. For this reason, both the G4UI data cards and the C++ class design reflects either a change to the nominal geometry due to an optimization (such as shortening the decay pipe length), or, conversely, a change in the geometry due to a misalignment, such as a transverse shift of the

Horn upstream (or downstream) alignment ball with respect to the nominal beam line.

1.3 Implementation

As hinted above, a set of C++ classes have been written to support the concept of a nominal geometry versus a controlled change, versus a misalignments. Those are introduced via the *LBNESurveyor* class, where simulated surveyed data can be entered via the G4UI data cards, and stored and retrieved when the corresponding mother volumes are ready to be declared to Geant4 Geometry modules. Although never used nor commissioned, a set of methods of the *LBNESurveyor* class allows to generate misalignments randomly, based on specified tolerance. An ensemble of realistic LBNE beam line can be generated that way, leading to a Monte-Carlo based method to quantify systematic uncertainties. The 2nd infrastructure class is named *LBNEVolmuePlacements*. The “Nominal” (i.e., corresponding to the baseline design, CD1, circa 2103) geometry is describes by dozens of volumes sizes and relative positions. However, such parameters can be modified via either a controlled change dictated via an optimization, or due to misalignment(s). Since - to our knowledge - there are no easy provisions to modify the Geant4 geometry once it is declared (and certainly not after it has been closed), a bookkeeping tool was deemed necessary and *LBNEVolmuePlacements* is it’s implementation. The constructor of this class contains all the declaration and initialization following the Baseline. Modification are allowed once the G4UI data cards corresponding to the “pre-init” stage are read in. Top level mother volume sizes and new locations are then set accordingly. Volumes whose size and location affects other parts (such as the Horn1 inner conductor and the target Helium container radius), are then defined, and stored in a collection of *LBNEVolmuePlacementData* objects. In the final phase of the G4 “detector construction” procedure, the geometry can be build “top-down”, or “inside-in”, i.e., largest volume first, small details later, using these objects¹

1.4 Further details

Top level elements (target, horns, decay pipe...) are located along a nominal beam line, with the origin, traditionally labeled “MCZERO”, close - but not exactly - at the entrance of Horn1. The integration drawing 8875.0000-ME-363028 and references therein was used to set this up. Since the entire beamline is left-right symmetric - ignoring misalignments, right-handedness is of no concern. Hard coded physical size or positions “hard-coded” in

¹One could have used the “inside-out”, small volume first, largest container last. This way of building a Geant4 geometry was introduced after the basic Geant4 geometry were designed. However, the present authors were not familiar with it. Moreover, it does not resolve constraints for volume found at the same levels of the volume hierarchy. Finally, one also wish to preserve the concept of a predefined “nominal beam line”, with well defined locations. Hence, the extra level of complexity described above was deemed necessary.

the C++ constructors do refer to various drawings of LBNE Docdb notes, in the form of C++ comments. The electronic repository of engineering drawings from the Accelerator Div. Mechanical Dept [?], *I-Find* has been extensively used throughout the coding period, tediously entering details such as the thin spider web supporting the inner conductor from the outer one. The entrance of Horn1 and the target is the most intricate part of the setup. In addition, the longitudinal position of the target with respect to Horn1 can be altered via either an “optimization” data card, or new transverse positions from the *LBNESurveyor*. Because this target is inserted into the upstream section of Horn1, the upstream and downstream sections do have different G4 mother volumes. Such a complex volume hierarchy could have been avoided, however, we concerned about G4 tracking performance when designing the G4 geometry. Prior to placing the G4 volumes, the *LBNEVolmuePlacements* has utilities to detect volumes overlaps, or mechanical tolerances on gaps are not satisfied. This can easily occur when the target or the horn are misaligned. For instance, the code will not run if the target is inserted to far into Horn1. Finally, a preliminary set of options to optimize the design of the horns system have been implemented, and partly commissioned. One can rescale the transverse or longitudinal dimension of each horn. So far, our focus has been on setting up the geometry. Other aspects of the g4lbne-v2 application have been preserved, such as the generation of the neutrino N-Tuple, and the Horn’s magnetic field calculations, including effects due to the skin depth for the horn’s inner conductors.

1.5 Inline Documentation

As stated above, run time specific options are implemented based on the G4UI package. Since the G4lbne-v3 executable can run either in a batch (for instance, on the FermiGrid), or interactively. The G4UI (both native to G4, or defined in the g4lbne-v3 package) data cards are organised into hierarchical directories. and can be browsed from the command line. Some guidance on how to change a parameter can then be decipher. For instance, a interactive session transcript could be:

```
<lbnegpvm02> ./g4lbne*****
```

Example of sets of data cards are provided along with the source code, allowing the users to insert a set of changes. Informal training via e-mail was found to be adequate, with specific consulting sessions and user-input on setting up these data cards.

1.6 Commissioning and validation

In addition to checks done in *LBNEVolmuePlacements*, all volumes are uploaded into the G4 geometry are checked for volume overlaps (i.e. using the method *G4PVPlacement::checkOverlaps*).

However, this check might still miss overlaps in few corners, justifying the checks done prior to the placements. Two distinct ways of checking the geometry have been extensively used. The first one is based on the G4 visualization tools. An example is shown on figure ??, showing details of the target. Surfaces, lines or corners that could be understood were investigated by collaborators that did not wrote the g4lbne-v3 code, discussed in the group, and issues were resolved, one by one. The second method is based on the G4 “tracking/stepping” debugging tools. So called “Geantino”² were send through the geometry, and specific track/volume intersections were recorded and compared to what’s expected, based on the engineering drawings.

2 Procedure for Evaluating Systematic Uncertainties

In all cases, we evaluate the uncertainty on the muon neutrino flux at the near detector, at the far detector, and on the near/far flux ratio between 0 and 10 GeV in bins of 0.5 GeV. For most sources of alignment uncertainty, we follow the following procedure:

- The flux at the near and far detectors in the nominal beam configurations is estimated using the simulation described in Section 1.
- The near and far detector fluxes are also estimated for several values of misalignment of a beamline parameter (e.g. offsets of Horn 1).
- The fractional change in the near detector flux, far detector flux and near/far flux ratio are calculated as a function of energy for each value of misalignment.
- In each 0.5 GeV energy bin, the dependence of the fractional change in flux (or flux ratio) on the amount of misalignment is extracted using fits that assume either a linear or a parabolic dependence on the amount of misalignment.
- The systematic uncertainty is extracted from the fit functions evaluated at the tolerance of quantity in question (see Table 1). The linear or parabolic fit is chosen based on which has the lowest χ^2 value.

This procedure, which closely follows a similar study performed for the NuMI beamline [?], is used to evaluate all of the alignment uncertainties listed in Table 1 except for baffle scraping and shielding block alignment. An example is shown in Figure 2, where the points show the fractional change in the near over far flux ratio for various shifts of the target position along the x axis. The fits to each energy bin are shown in Figure 2, and the results of the

²A type of G4 particles that have no electric charge, and perfectly sterile regarding interaction with the material

fit are shown by the solid lines in Figure 2. The total error, estimated by evaluating the fits at the target position tolerance of 0.5 mm, is shown in Figure 2. Plots of varied fluxes and fits for other alignment parameters are available in Appendices ??- ??.

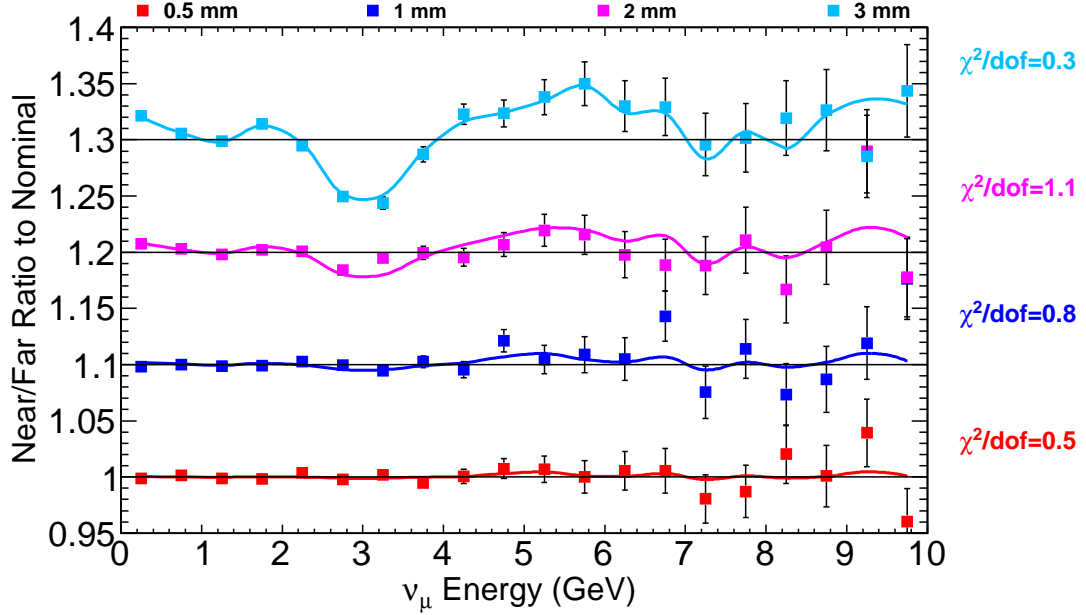


Figure 1: Near/Far double ratios to nominal for several values of **Target Offset in x** (points) and the results of the fits to each energy bin (lines).

To study the effect of shielding block alignment, we have simulated the flux with and without shielding blocks present. The ratio of these is shown for the near detector in Figure 2 and for the far detector in Figure 2. We find no difference from the nominal configuration beyond statistical fluctuations. We therefore assume that alignment block shifts of order 1 cm would lead to negligible systematic uncertainties and do not include this source in our total estimat of alignment uncertainties.

For the baffle scraping uncertainty, we estimate the flux from the baffle by simulating a point-like beam fired directly at the baffle. Specifically, we simulate a beam with a 0.001 mm standard deviation in width and height offset from the origin by 7 mm. The flux resulting from aiming the beam at several positions on the baffle in shown in figure 2. We then estimate baffle uncertainty by taking 0.25

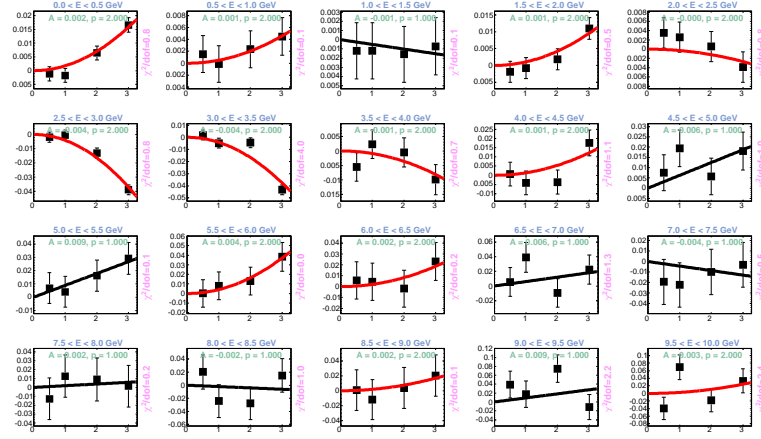


Figure 2: Fits to the near/far ratios for several values of **Target Offset in x** . Black(Red) fit lines indicate that a linear(parabolic) fit provided the best χ^2 .

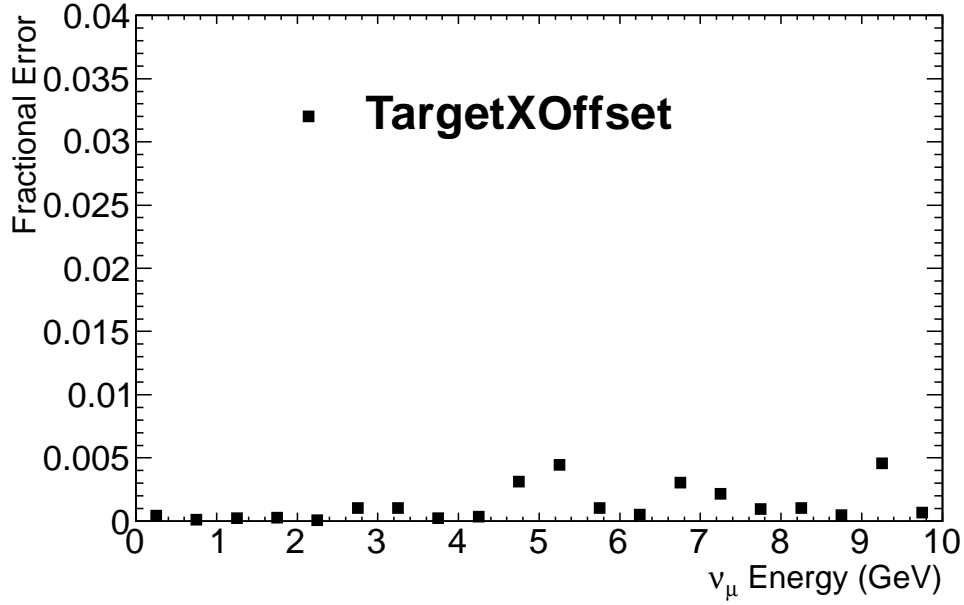


Figure 3: Systematic uncertainty on the near/far flux ratio due to a target offset along the x axis.

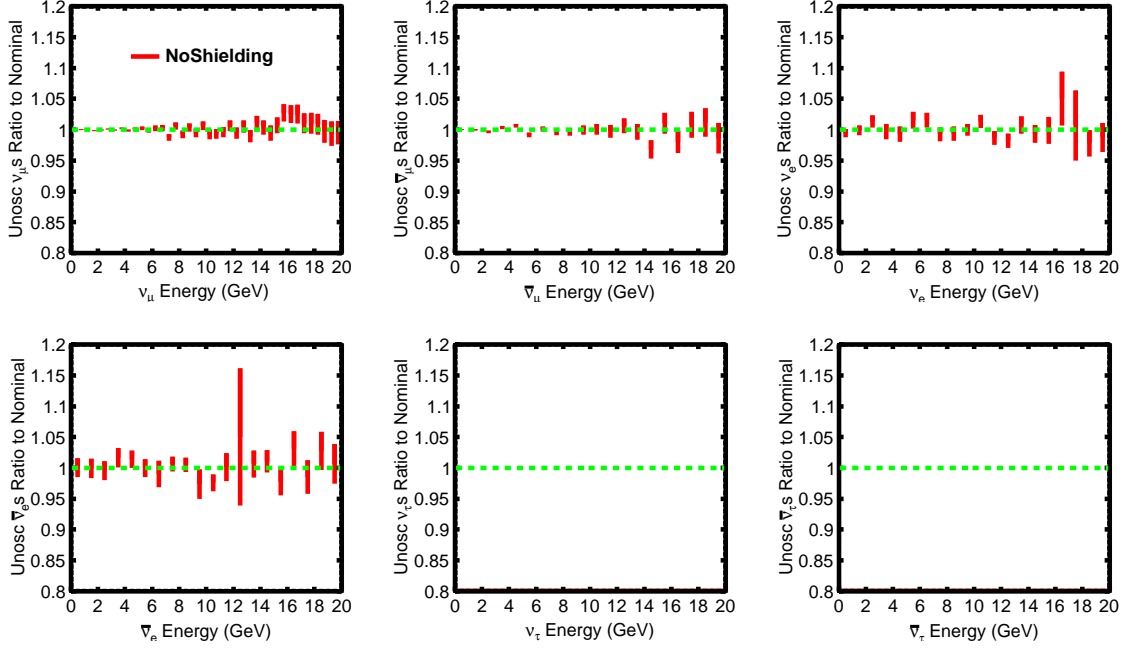


Figure 4: The ratio of flux in the near neutrino detector without shielding blocks to the nominal flux produced with shielding blocks included in the geometry simulation.

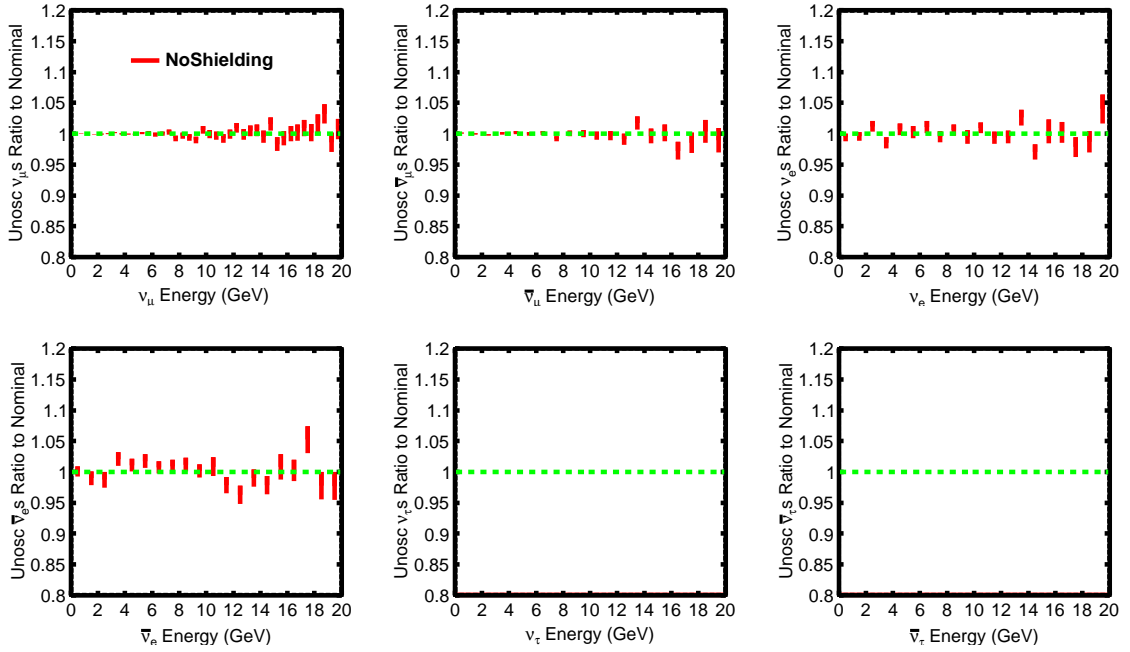


Figure 5: The ratio of flux in the far neutrino detector without shielding blocks to the nominal flux produced with shielding blocks included in the geometry simulation.

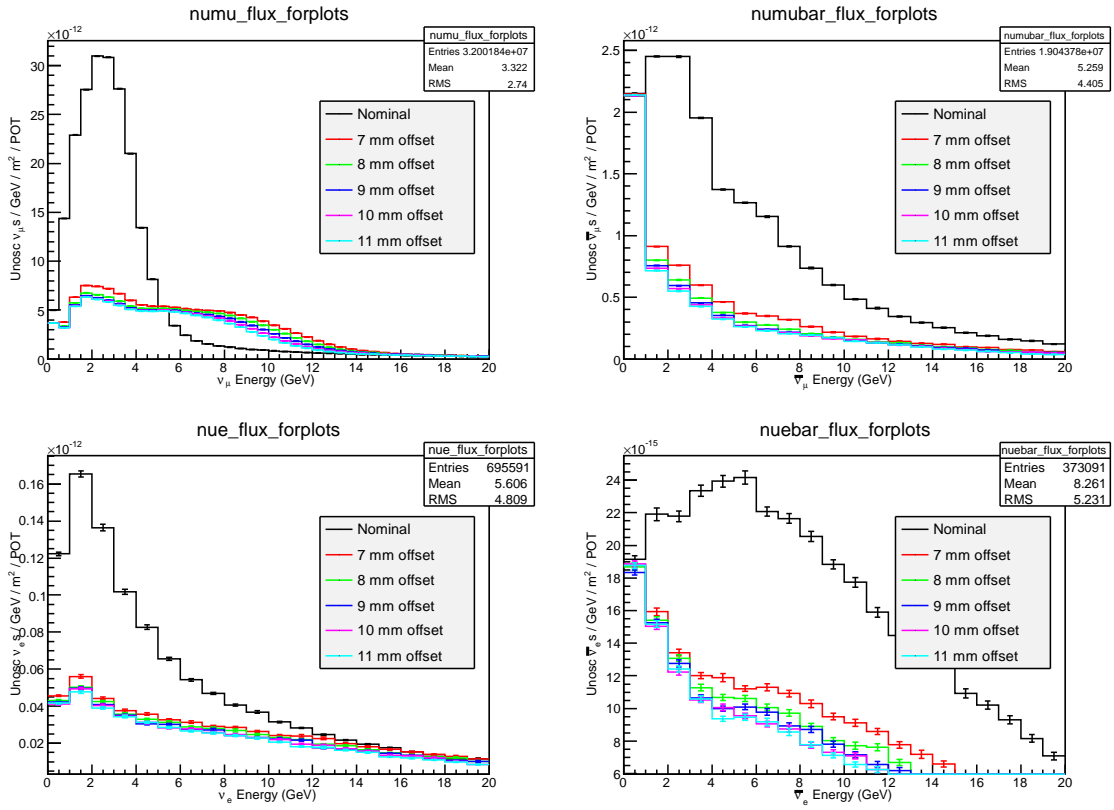


Figure 6: Fluxes at the far detector in the nominal configuration (with the centered on the graphite target) and with the beam directed at various points on the baffle.

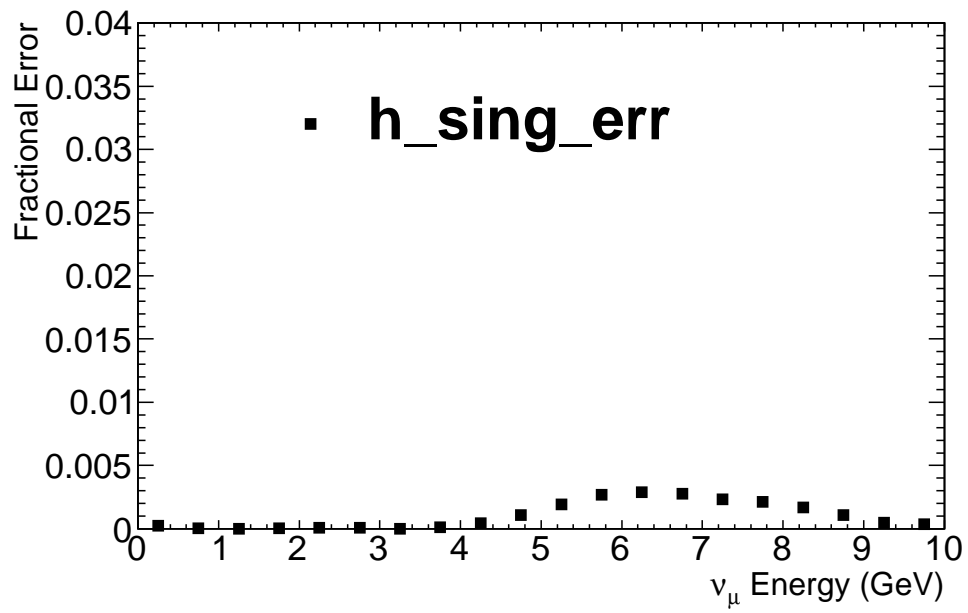


Figure 7: Systematic uncertainty on the near/far flux ratio due to baffle scraping.

3 Results

Table 2: Alignment Error Summary

Energy(GeV)	0-0.5	0.5-1	1-1.5	1.5-2	2-2.5	2.5-3
Far Det Offset X	1.43914e-05	3.38222e-05	7.59571e-05	2.42739e-07	3.69186e-05	3.73595e-05
Far Det Offset Y	2.06246e-05	3.70303e-05	6.53186e-05	2.52197e-07	4.30858e-05	4.16559e-05
Near Det Offset X	0.000101184	2.70841e-06	1.09669e-05	0.000181531	7.00454e-05	1.94171e-05
Near Det Offset Y	0.000102205	2.94374e-06	1.07677e-05	0.000173899	5.26796e-05	1.67149e-05
Horn Current	0.00042769	0.000330626	0.000134498	0.000181768	0.000410885	0.0019110
Horn 1 X Tilt	0.000181934	7.83654e-05	0.000101032	5.40829e-06	0.000218009	0.0002884
Horn 1 Y Tilt	0.000271695	4.63918e-05	0.000109269	1.63758e-05	0.000608306	2.18061e-05
Horn 1 X Offset	9.90654e-05	2.04572e-05	5.10141e-05	0.000138626	0.000101709	0.0008987
Horn 1 Y Offset	0.000229221	5.22704e-06	0.000226962	2.61067e-05	2.88124e-06	0.0001578
Horn 2 X Offset	0.000130758	2.40259e-05	0.000164589	0.000276573	0.000203388	0.0001555
Horn 2 Y Offset	7.01115e-06	4.05838e-05	1.0772e-05	5.27883e-05	8.20463e-05	8.91907e-05
Horn 2 X Tilt	5.28111e-06	3.76531e-05	1.88892e-05	2.10732e-05	0.000376106	4.55912e-05
Horn 2 Y Tilt	1.78469e-05	0.000121235	1.88028e-05	4.09452e-05	0.00018725	0.0001147
Target X Offset	0.000440168	0.00012732	0.000254436	0.000265967	7.42663e-05	0.0010280
Target Y Offset	1.69563e-05	8.59897e-05	0.000152945	8.30214e-05	0.000110642	0.0002087
Target X Tilt	0.000336972	0.000100614	8.10728e-05	0.000706322	5.12143e-05	0.0008292
Target Y Tilt	0.000146855	9.48196e-05	6.65269e-05	4.55779e-05	1.87778e-05	0.0005177
Beam Width X	0.00124628	0.000378573	2.15325e-05	0.000190355	2.45415e-05	2.95214e-05
Beam Width Y	1.5959e-05	2.68322e-05	0.000135738	0.000192648	0.000319397	3.95301e-05
Decay Pipe Radius	0.00220006	0.00812896	0.0109963	0.0015003	0.00844544	0.0090330
Water Layer Thickness	0.000987118	0.000247876	0.000108067	0.000944201	0.00033889	0.0018030
	0.0153622	0.00438478	0.00290503	0.00590875	0.00768252	0.0076788
Decay Pipe Shift X	5.02719e-05	1.06952e-06	1.03525e-05	2.85398e-05	3.14974e-06	1.75653e-05
IC Skin Depth	0.000333299	0.000291878	0.000498095	0.000846566	0.000932064	0.0008861
BeamTilt X	8.56579e-06	3.74113e-05	2.07974e-05	2.92056e-06	2.30787e-05	4.63765e-05
BeamTilt Y	1.04139e-05	1.8403e-06	3.16983e-05	2.59203e-05	1.58252e-06	5.39003e-05
Beam Offset X	0.00173775	0.000558719	0.000245785	0.000626451	0.000403351	0.0002225
Beam Offset Y	0.000102958	8.54086e-05	2.03301e-06	6.30912e-05	2.22532e-05	0.001064

labeltab:errorssummary

[ht]

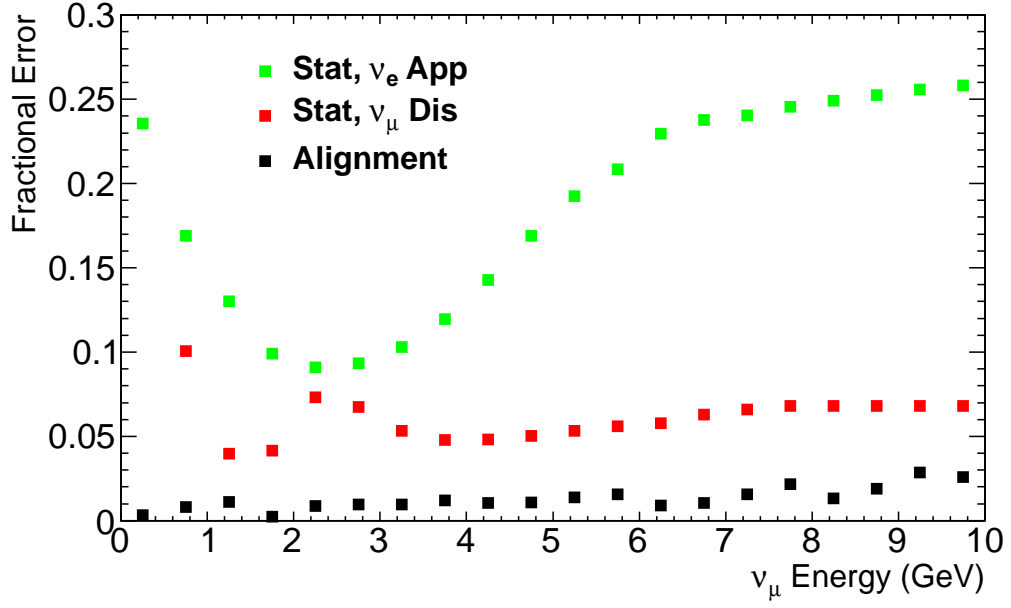


Figure 8: Total fractional alignment systematic uncertainty as a function of energy on the near/far flux ratio.

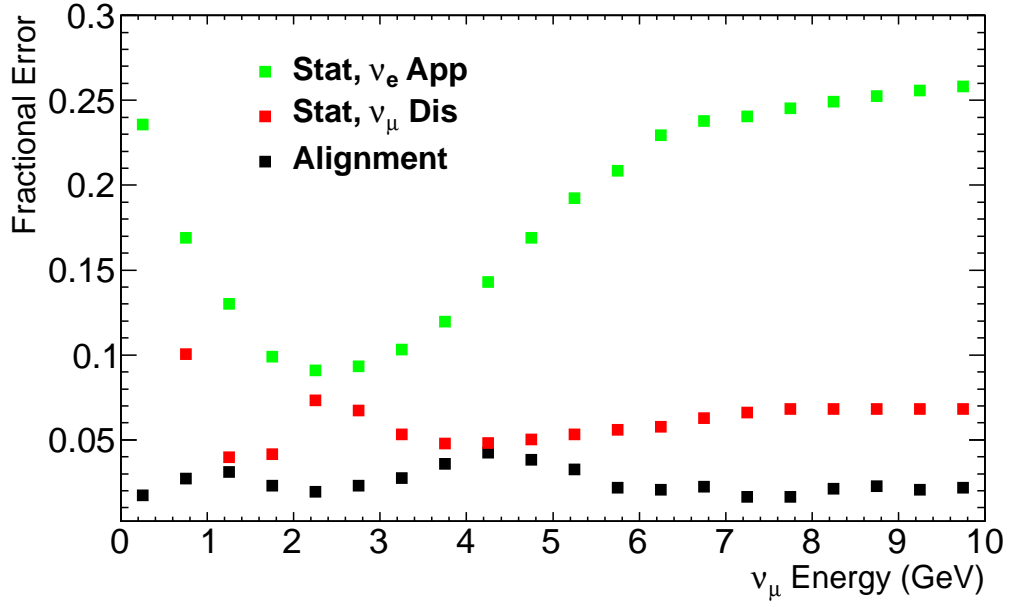


Figure 9: Total fractional alignment systematic uncertainty as a function of energy on the flux at the near detector.

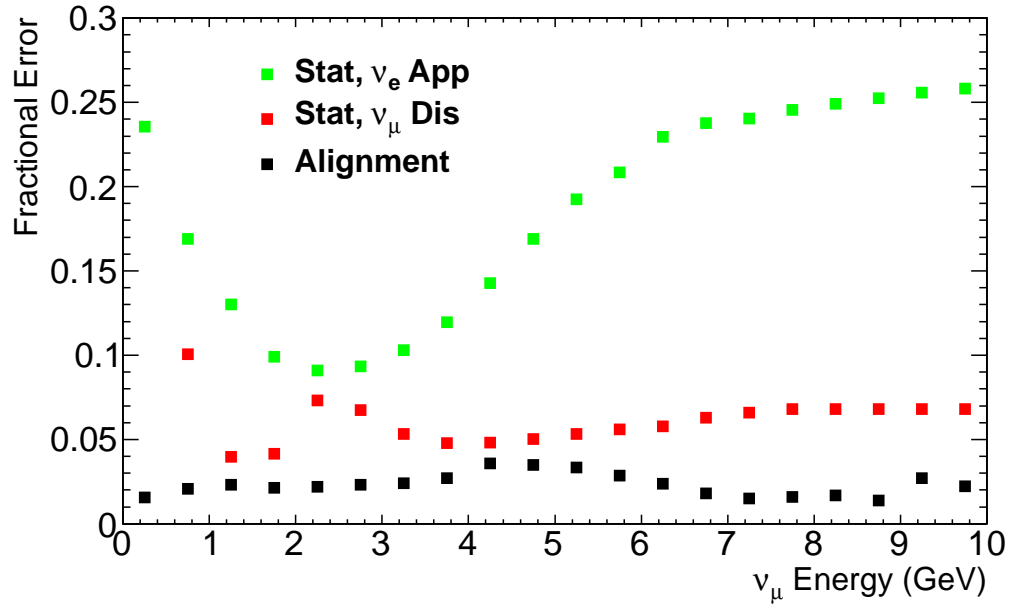


Figure 10: Total fractional alignment systematic uncertainty as a function of energy on the flux at the far detector.

Figure 11: Summary of alignment systematic uncertainties on the near/far flux ratio.

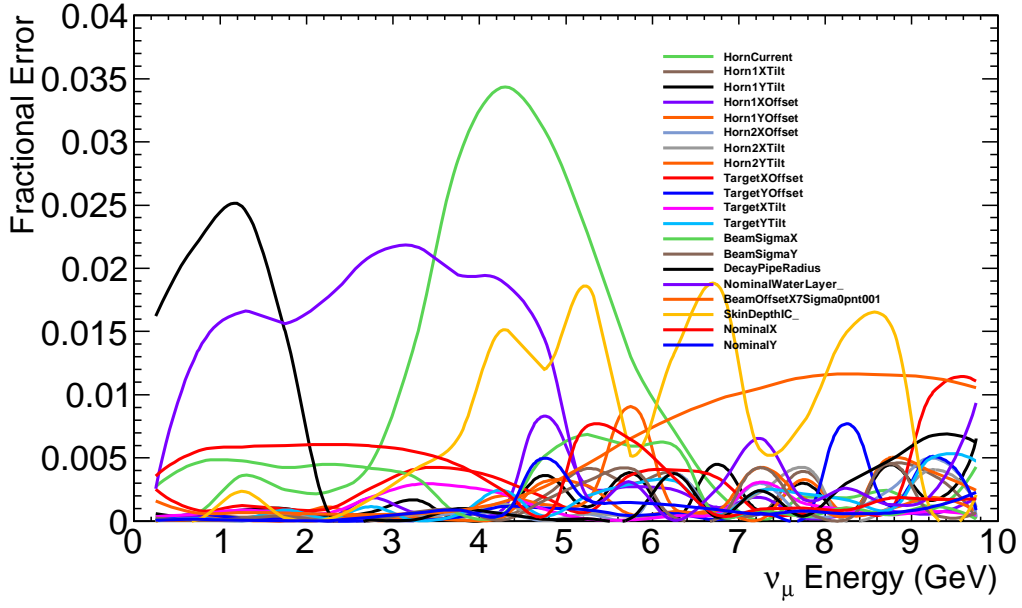


Figure 12: Summary of alignment systematic uncertainties on the flux at the near detector.

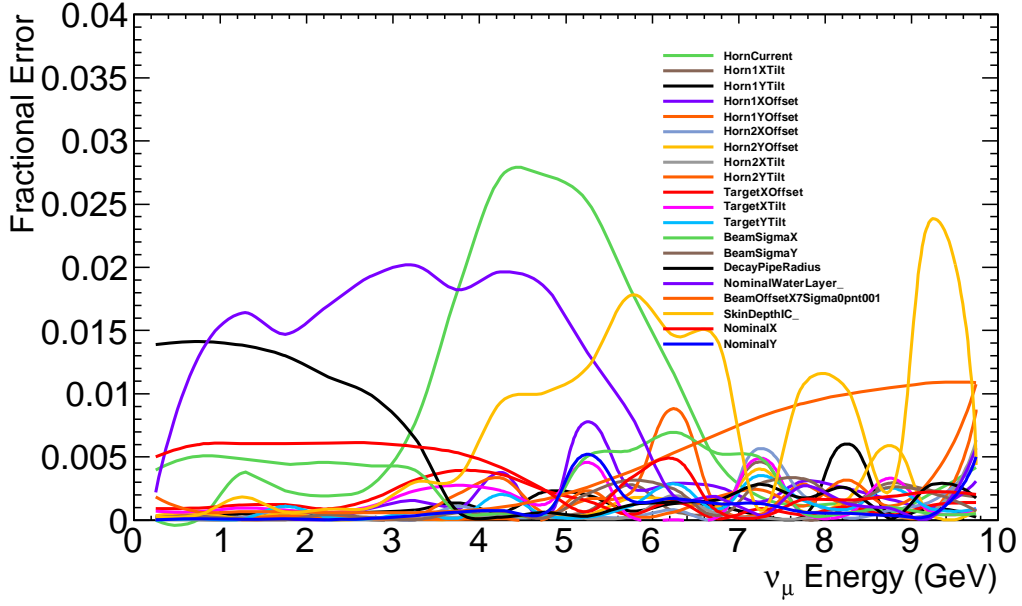


Figure 13: Summary of alignment systematic uncertainties on the flux at the far detector.

4 Conclusion

A Near/Far Flux Ratios and Fits

A.1 Target Position

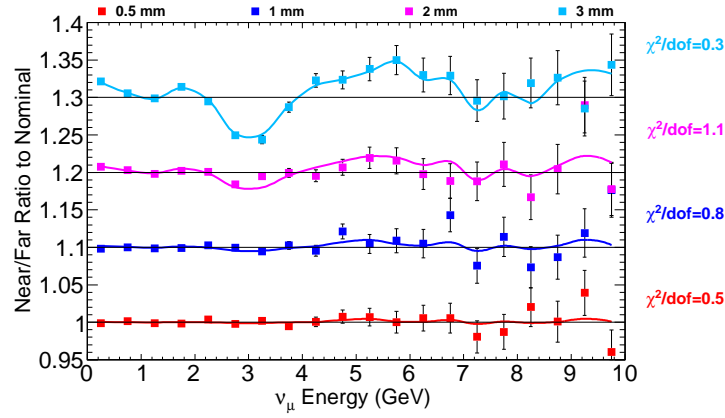


Figure 14: Near/Far double ratios to nominal for several values of **Target Offset in x** (points) and the results of the fits to each energy bin (lines).

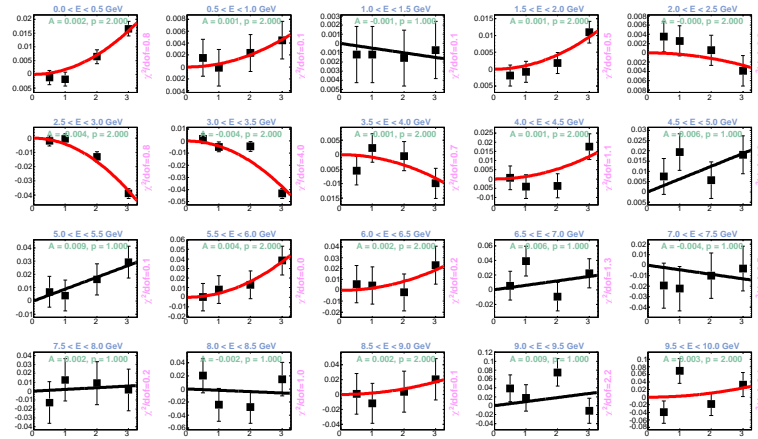


Figure 15: Fits to the near/far ratios for several values of **Target Offset in x** . Black(Red) fit lines indicate that a linear(parabolic) fit provided the best χ^2 .

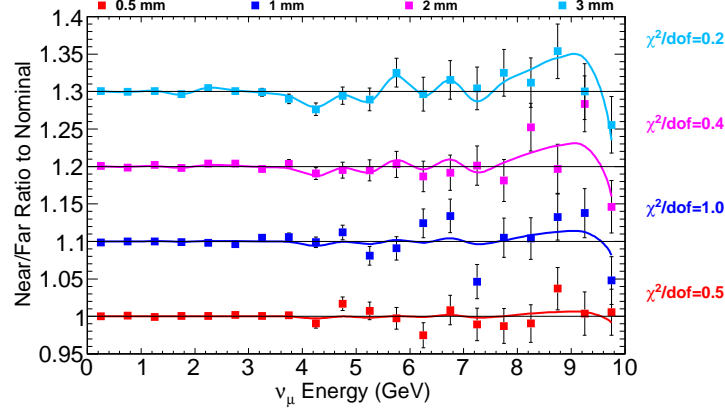


Figure 16: Near/Far double ratios to nominal for several values of **Target Offset in y** (points) and the results of the fits to each energy bin (lines).

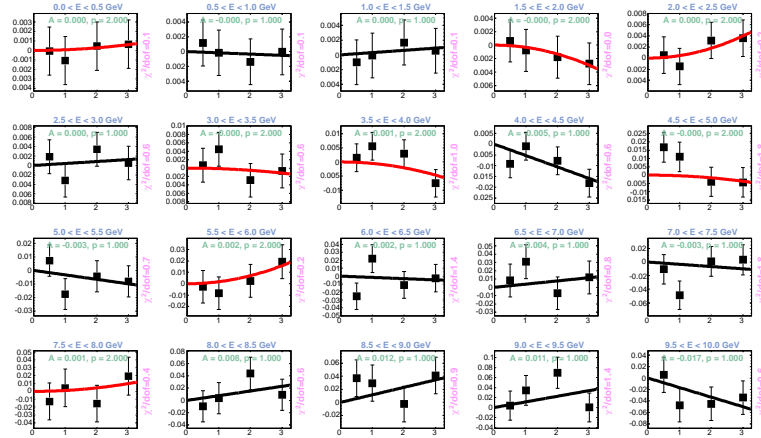


Figure 17: Fits to the near/far ratios for several values of **Target Offset in y** . Black(Red) fit lines indicate that a linear(parabolic) fit provided the best χ^2 .

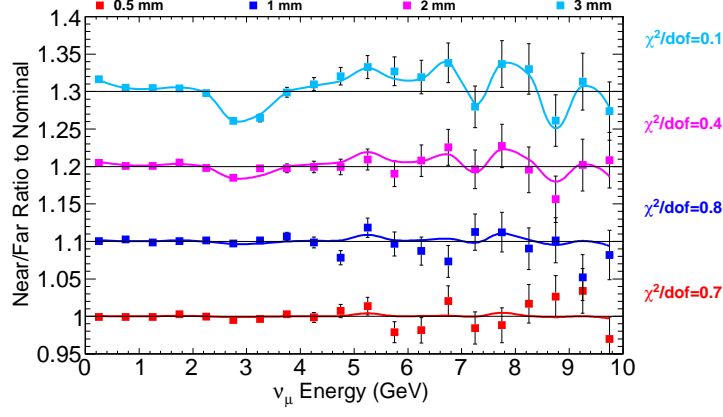


Figure 18: Near/Far double ratios to nominal for several values of **Target Tilt in x** (points) and the results of the fits to each energy bin (lines).

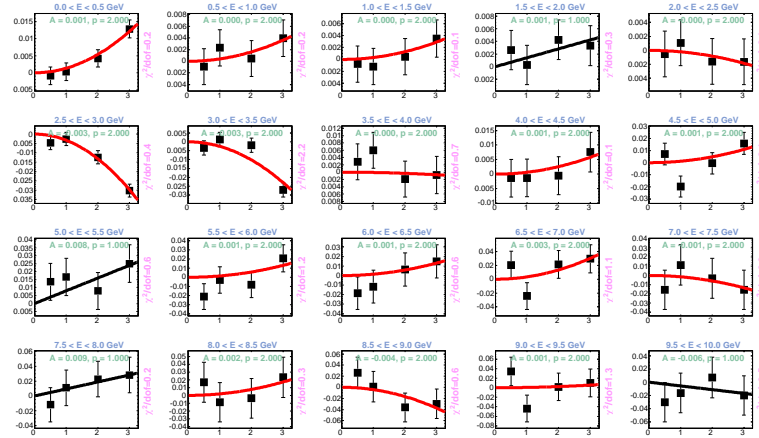


Figure 19: Fits to the near/far ratios for several values of **Target Tilt in x** . Black(Red) fit lines indicate that a linear(parabolic) fit provided the best χ^2 .

A.2 Horn 1 Position

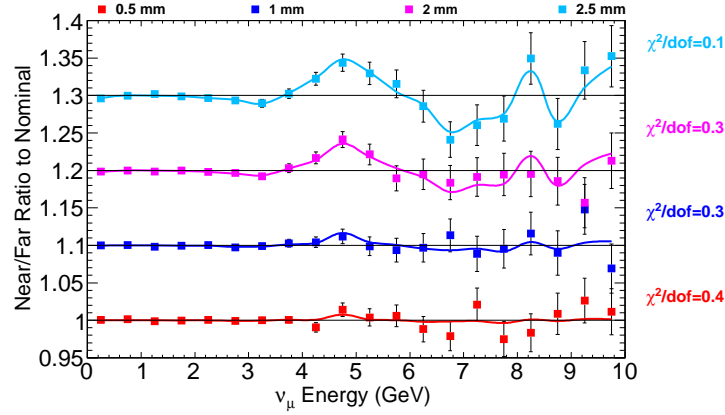


Figure 20: Near/Far double ratios to nominal for several values of **Horn 1 Offset in x** (points) and the results of the fits to each energy bin (lines).

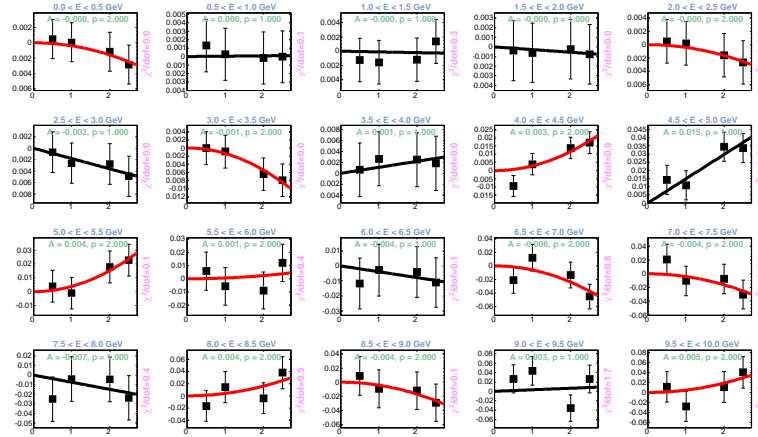


Figure 21: Fits to the near/far ratios for several values of **Horn 1 Offset in x** . Black(Red) fit lines indicate that a linear(parabolic) fit provided the best χ^2 .

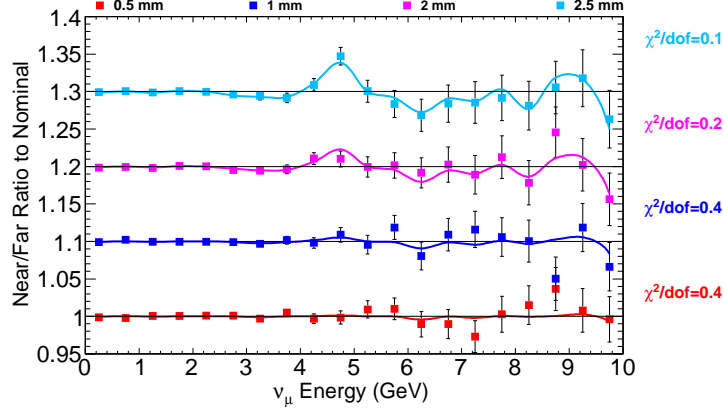


Figure 22: Near/Far double ratios to nominal for several values of **Horn 1 Offset in y** (points) and the results of the fits to each energy bin (lines).

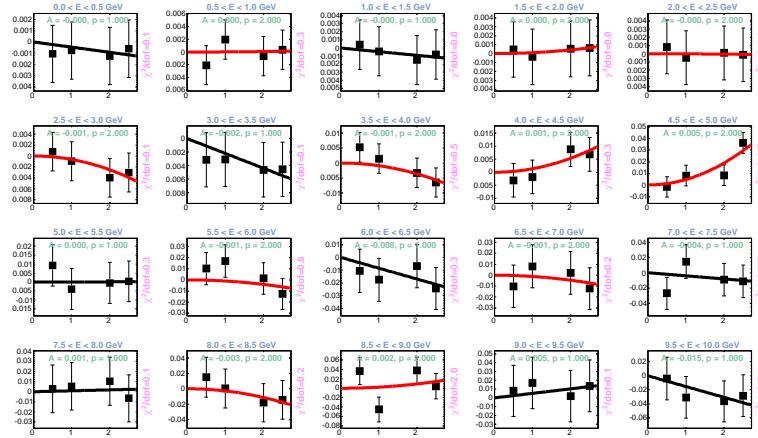


Figure 23: Fits to the near/far ratios for several values of **Horn 1 Offset in y** . Black(Red) fit lines indicate that a linear(parabolic) fit provided the best χ^2 .

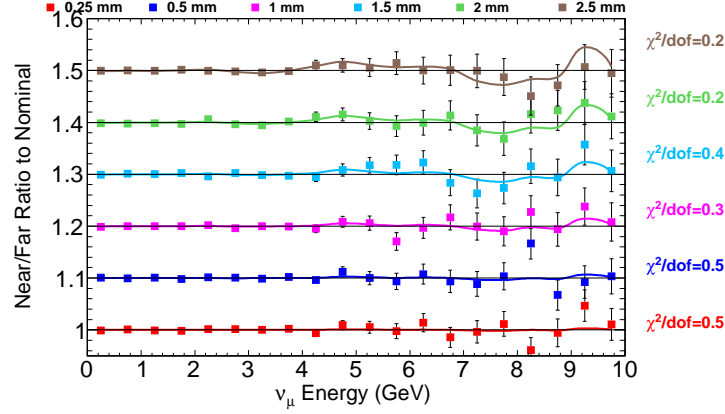


Figure 24: Near/Far double ratios to nominal for several values of **Horn 1 Tilt in x** (points) and the results of the fits to each energy bin (lines).

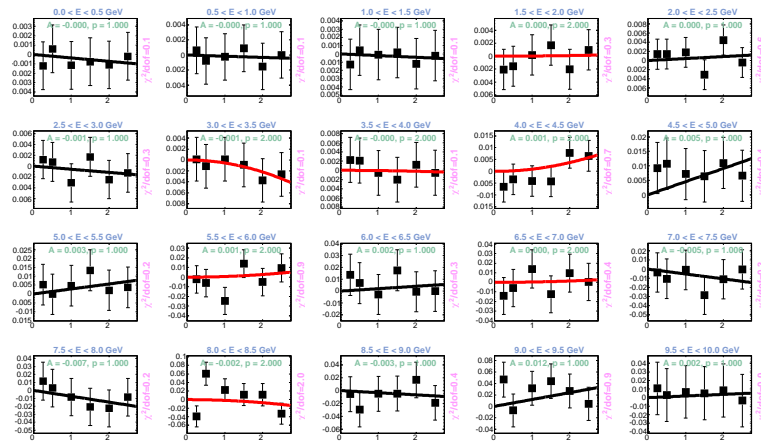


Figure 25: Fits to the near/far ratios for several values of **Horn 1 Tilt in x** . Black(Red) fit lines indicate that a linear(parabolic) fit provided the best χ^2 .

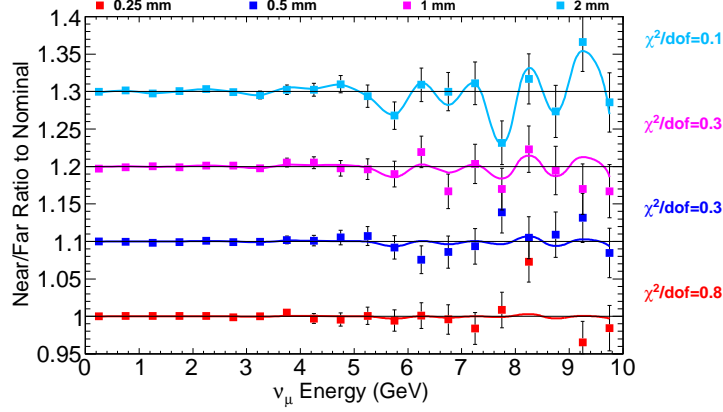


Figure 26: Near/Far double ratios to nominal for several values of **Horn 1 Tilt in y** (points) and the results of the fits to each energy bin (lines).

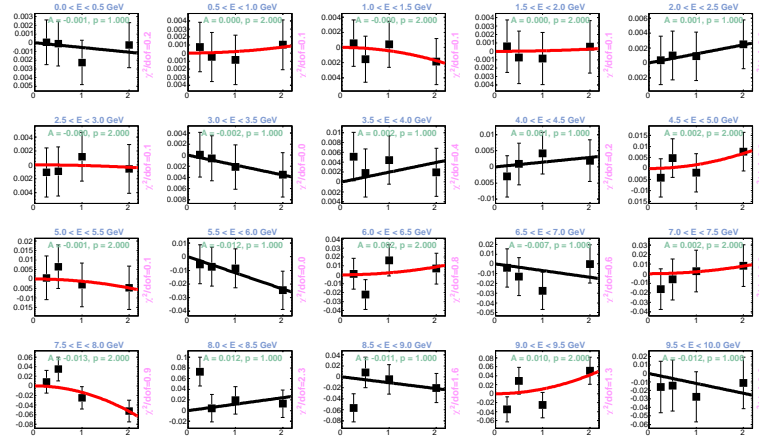


Figure 27: Fits to the near/far ratios for several values of **Horn 1 Tilt in y** . Black(Red) fit lines indicate that a linear(parabolic) fit provided the best χ^2 .

A.3 Horn 2 Position

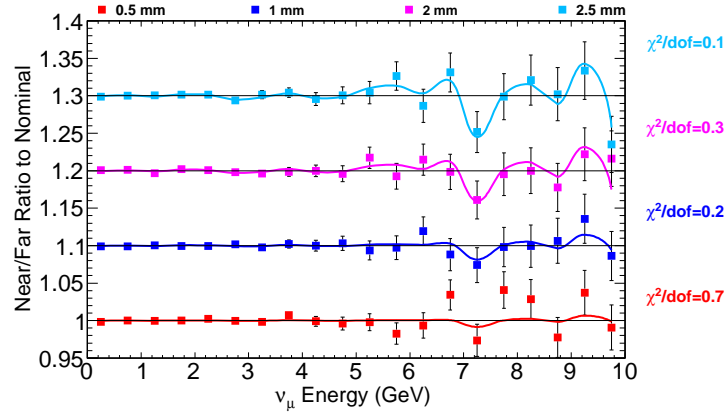


Figure 28: Near/Far double ratios to nominal for several values of **Horn 2 Offset in x** (points) and the results of the fits to each energy bin (lines).

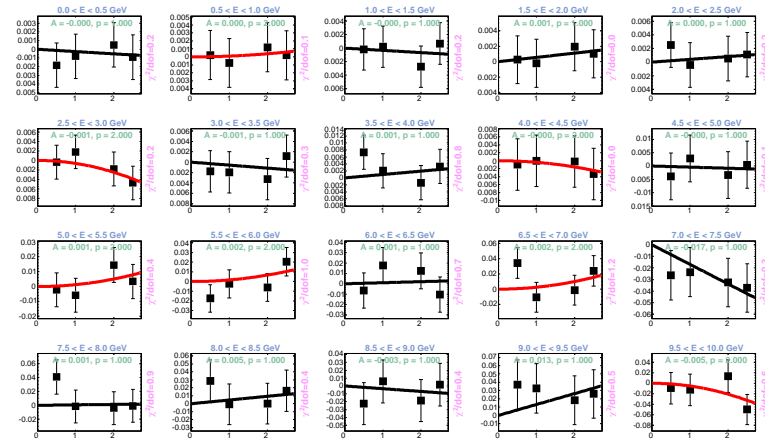


Figure 29: Fits to the near/far ratios for several values of **Horn 2 Offset in x** . Black(Red) fit lines indicate that a linear(parabolic) fit provided the best χ^2 .

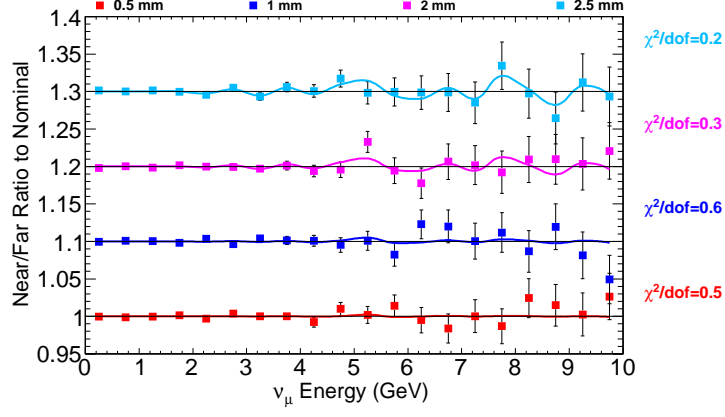


Figure 30: Near/Far double ratios to nominal for several values of **Horn 2 Offset in y** (points) and the results of the fits to each energy bin (lines).

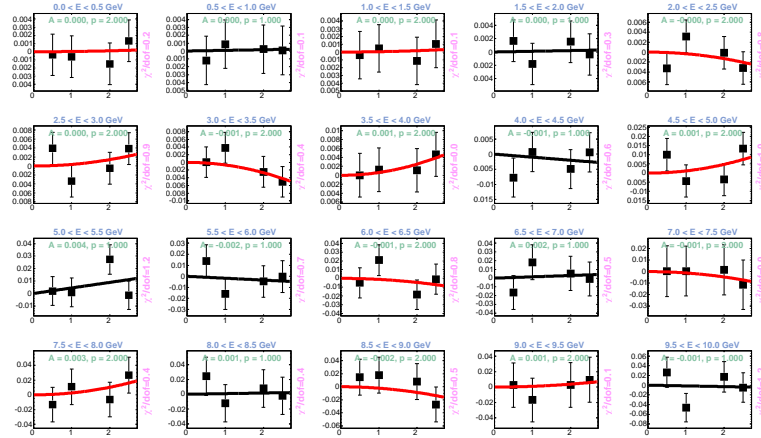


Figure 31: Fits to the near/far ratios for several values of **Horn 2 Offset in y** . Black(Red) fit lines indicate that a linear(parabolic) fit provided the best χ^2 .

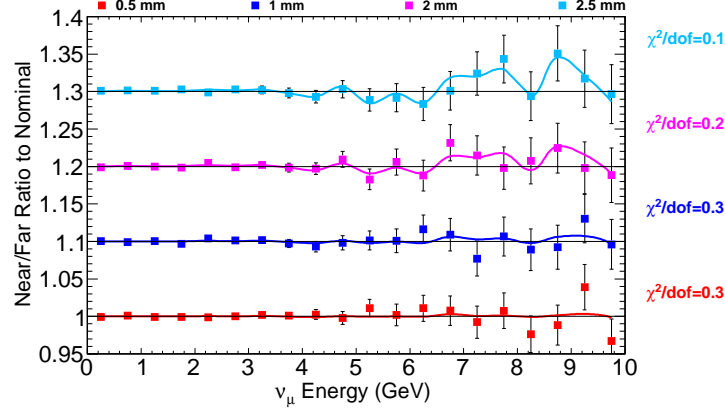


Figure 32: Near/Far double ratios to nominal for several values of **Horn 2 Tilt in x** (points) and the results of the fits to each energy bin (lines).

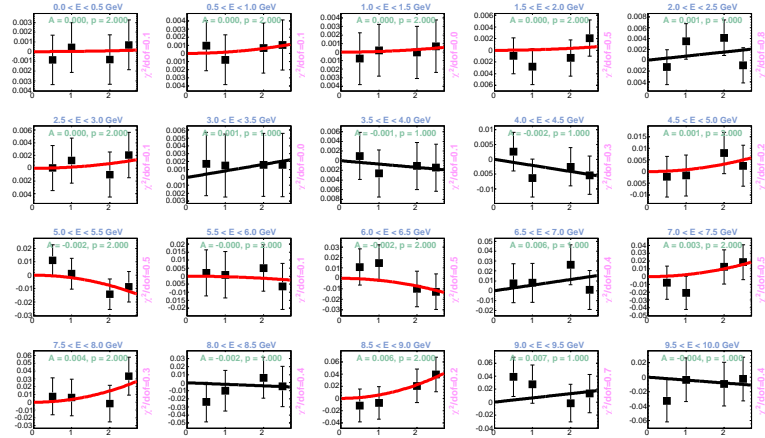


Figure 33: Fits to the near/far ratios for several values of **Horn 2 Tilt in x** . Black(Red) fit lines indicate that a linear(parabolic) fit provided the best χ^2 .

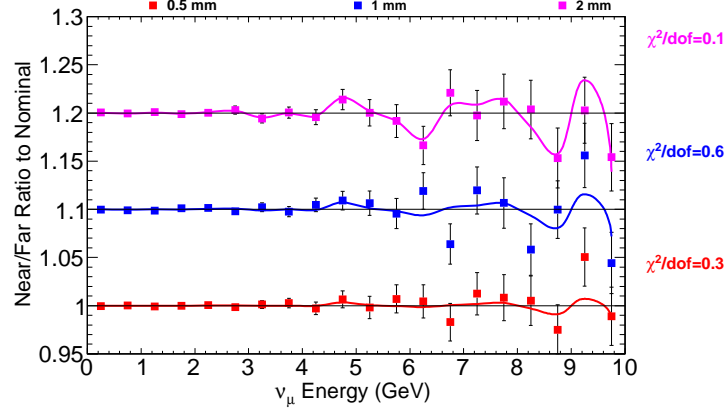


Figure 34: Near/Far double ratios to nominal for several values of **Horn 2 Tilt in y** (points) and the results of the fits to each energy bin (lines).

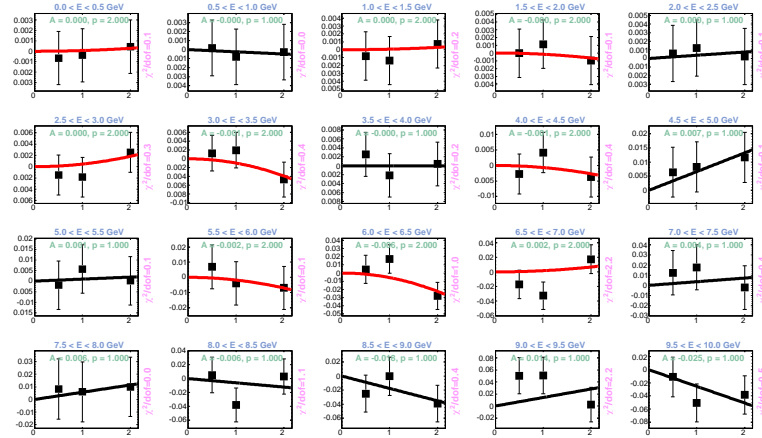


Figure 35: Fits to the near/far ratios for several values of **Horn 2 Tilt in y** . Black(Red) fit lines indicate that a linear(parabolic) fit provided the best χ^2 .

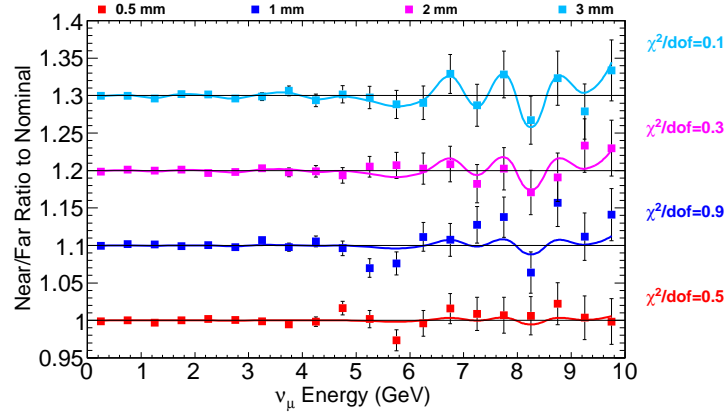


Figure 36: Near/Far double ratios to nominal for several values of **Target Tilt in y** (points) and the results of the fits to each energy bin (lines).

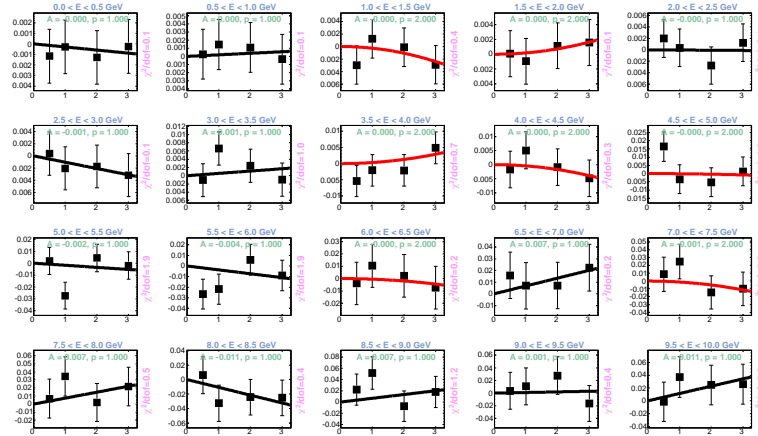


Figure 37: Fits to the near/far ratios for several values of **Target Tilt in y** . Black(Red) fit lines indicate that a linear(parabolic) fit provided the best χ^2 .

A.4 Far Detector Position

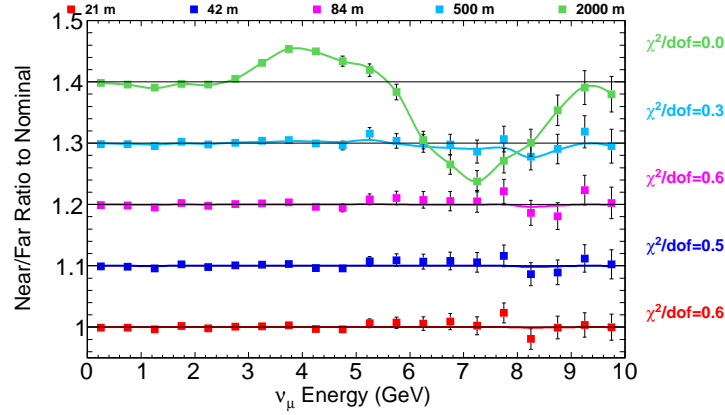


Figure 38: Near/Far double ratios to nominal for several values of **Far detector offset in x** (points) and the results of the fits to each energy bin (lines).

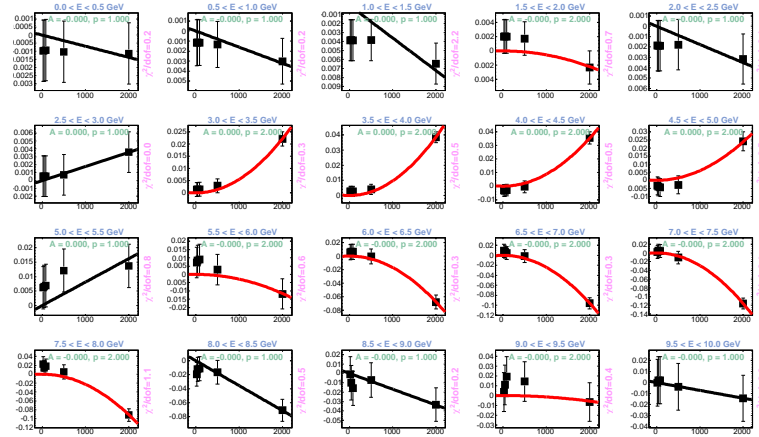


Figure 39: Fits to the near/far ratios for several values of **Far detector offset in x** . Black(Red) fit lines indicate that a linear(parabolic) fit provided the best χ^2 .

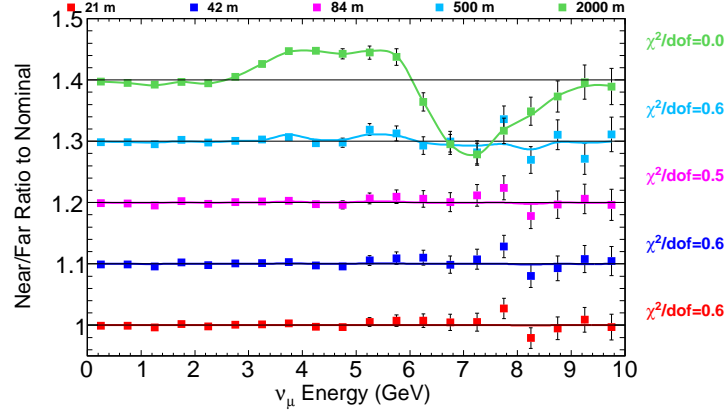


Figure 40: Near/Far double ratios to nominal for several values of **Far detector offset in y** (points) and the results of the fits to each energy bin (lines).

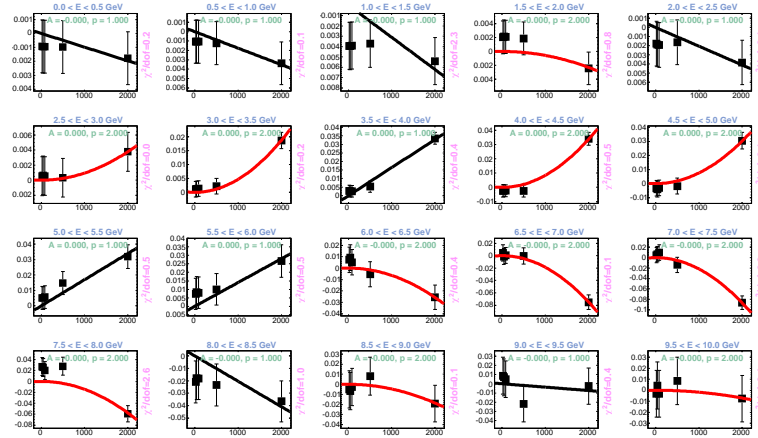


Figure 41: Fits to the near/far ratios for several values of **Far detector offset in y** . Black(Red) fit lines indicate that a linear(parabolic) fit provided the best χ^2 .

A.5 Decay Pipe Position

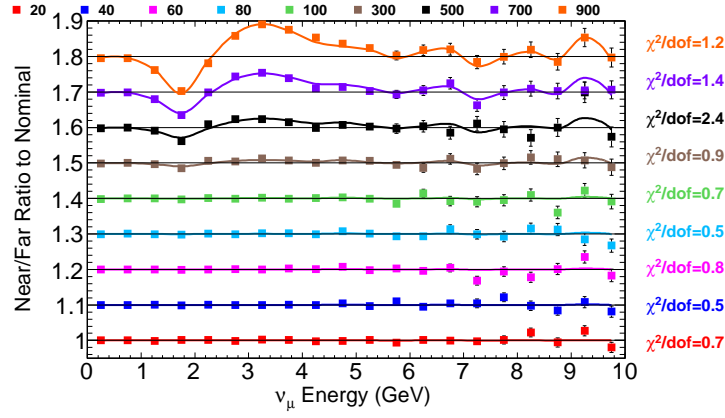


Figure 42: Near/Far double ratios to nominal for several values of **Decay Pipe Offset in x** (points) and the results of the fits to each energy bin (lines).

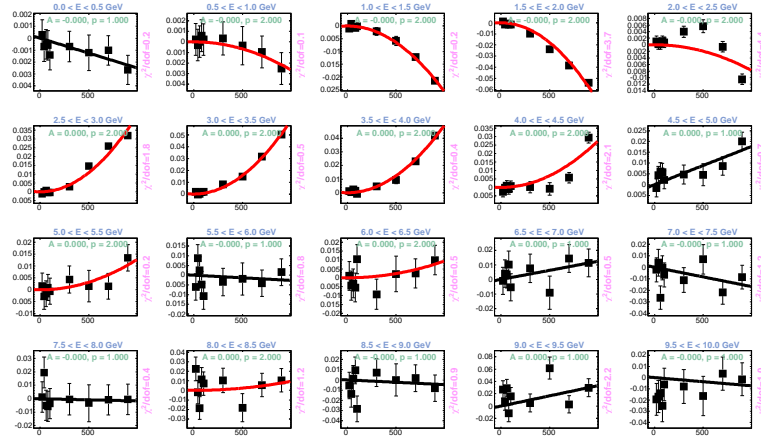


Figure 43: Fits to the near/far ratios for several values of **Decay Pipe Offset in x** . Black(Red) fit lines indicate that a linear(parabolic) fit provided the best χ^2 .

A.6 Decay Pipe Radius

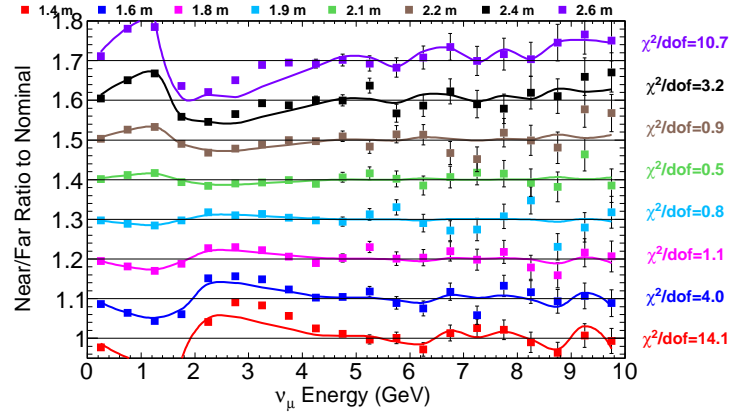


Figure 44: Near/Far double ratios to nominal for several values of **Decay Pipe Radius** (points) and the results of the fits to each energy bin (lines).

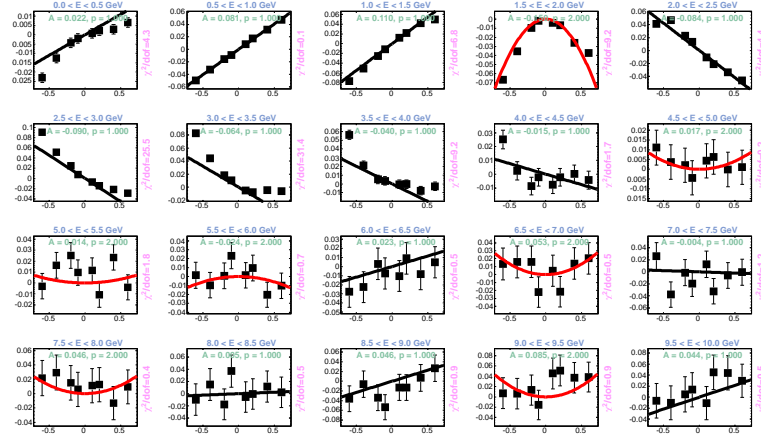


Figure 45: Fits to the near/far ratios for several values of **Decay Pipe Radius**. Black(Red) fit lines indicate that a linear(parabolic) fit provided the best χ^2 .

A.7 Horn Current

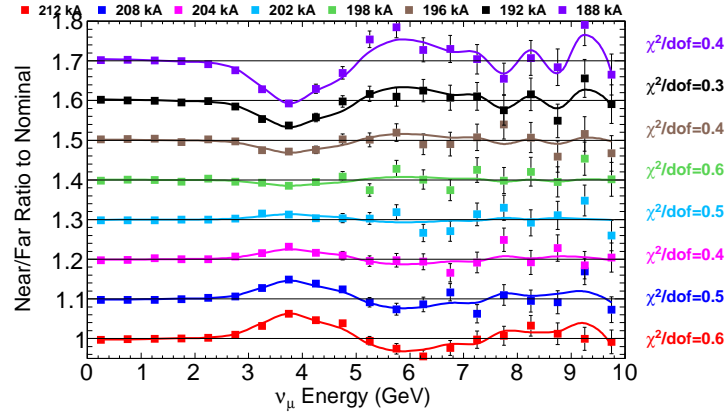


Figure 46: Near/Far double ratios to nominal for several values of **Horn Current** (points) and the results of the fits to each energy bin (lines).

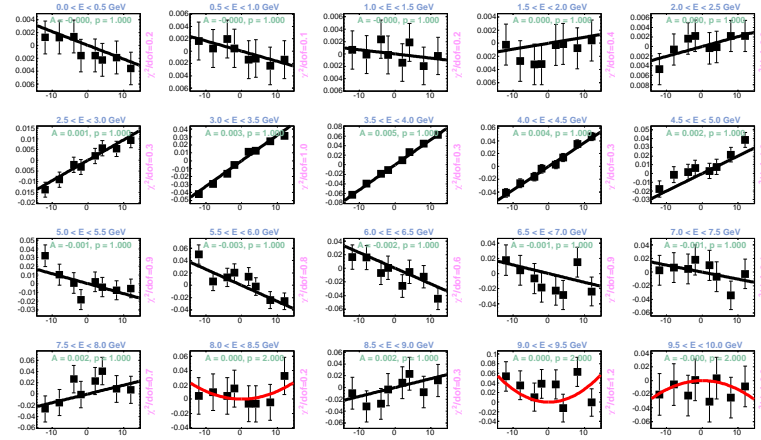


Figure 47: Fits to the near/far ratios for several values of **HornCurrent**. Black(Red) fit lines indicate that a linear(parabolic) fit provided the best χ^2 .

A.8 Horn Water Layer Thickness

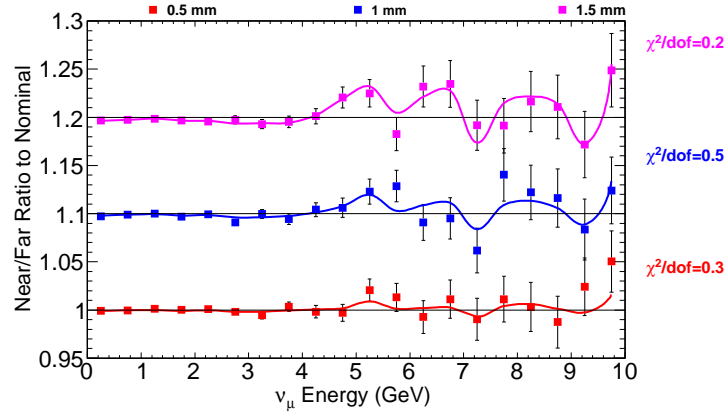


Figure 48: Near/Far double ratios to nominal for several values of **horn cooling water layer thickness** (points) and the results of the fits to each energy bin (lines).

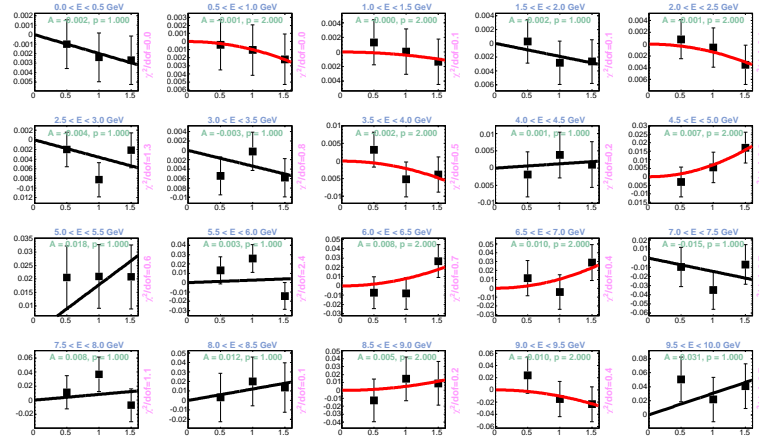


Figure 49: Fits to the near/far ratios for several values of **horn cooling water layer thickness**. Black(Red) fit lines indicate that a linear(parabolic) fit provided the best χ^2 .

A.9 Beam size at target

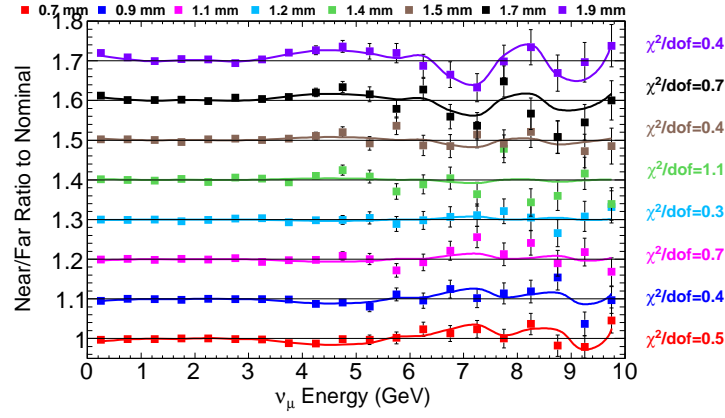


Figure 50: Near/Far double ratios to nominal for several values of **Beam size in x** (points) and the results of the fits to each energy bin (lines).

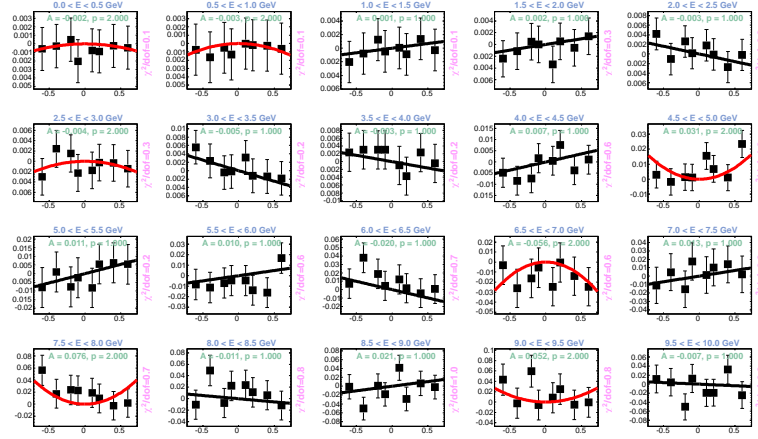


Figure 51: Fits to the near/far ratios for several values of **Beam size in x** . Black(Red) fit lines indicate that a linear(parabolic) fit provided the best χ^2 .

A.10 Beam Position at Target

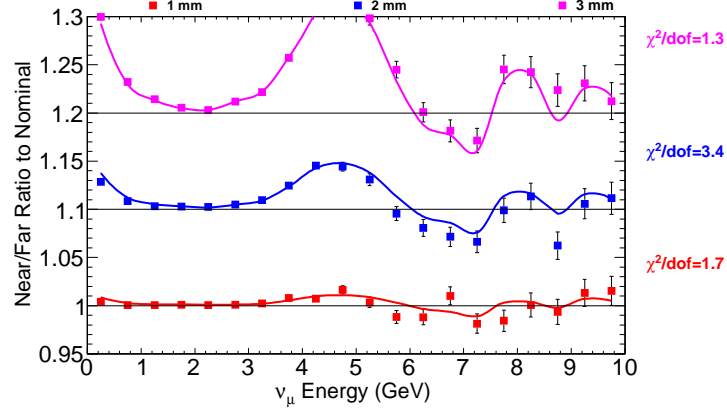


Figure 52: Near/Far double ratios to nominal for several values of **Beam x offset at target** (points) and the results of the fits to each energy bin (lines).

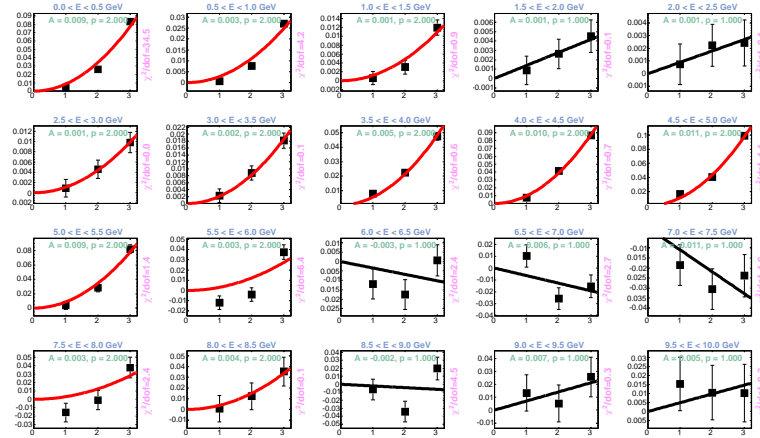


Figure 53: Fits to the near/far ratios for several values of **Beam x offset at target**. Black(Red) fit lines indicate that a linear(parabolic) fit provided the best χ^2 .

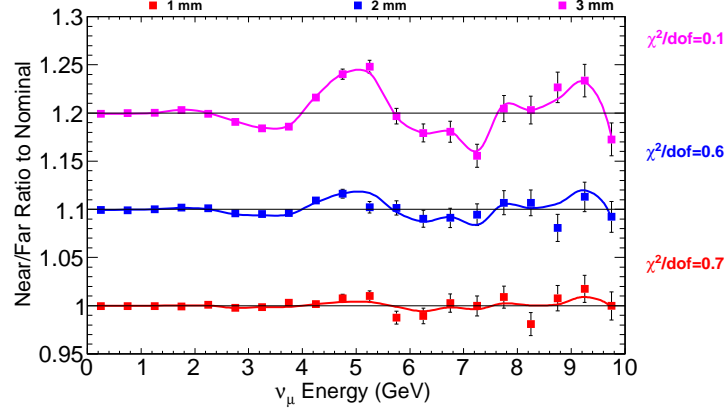


Figure 54: Near/Far double ratios to nominal for several values of **Beam y offset at target** (points) and the results of the fits to each energy bin (lines).

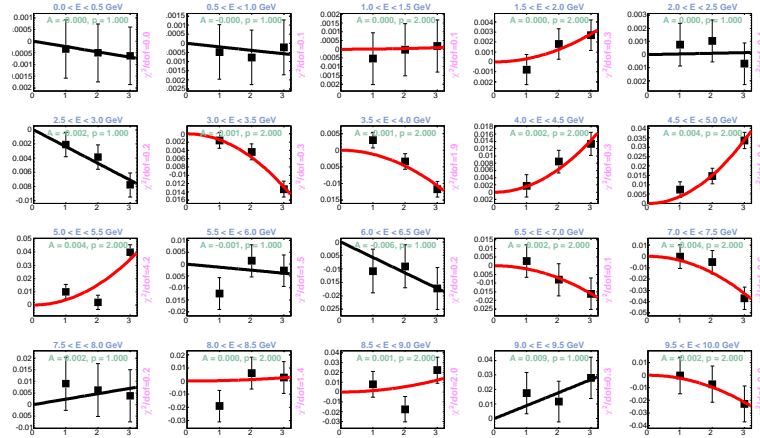


Figure 55: Fits to the near/far ratios for several values of **Beam y offset at target**. Black(Red) fit lines indicate that a linear(parabolic) fit provided the best χ^2 .

A.11 Beam Angle at Target

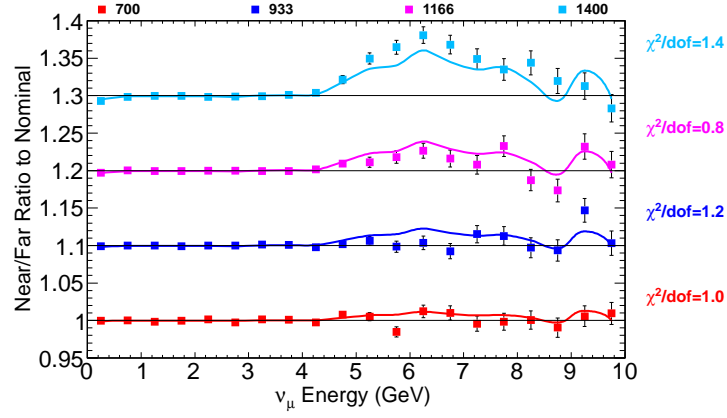


Figure 56: Near/Far double ratios to nominal for several values of **beam tilt in x** (points) and the results of the fits to each energy bin (lines).

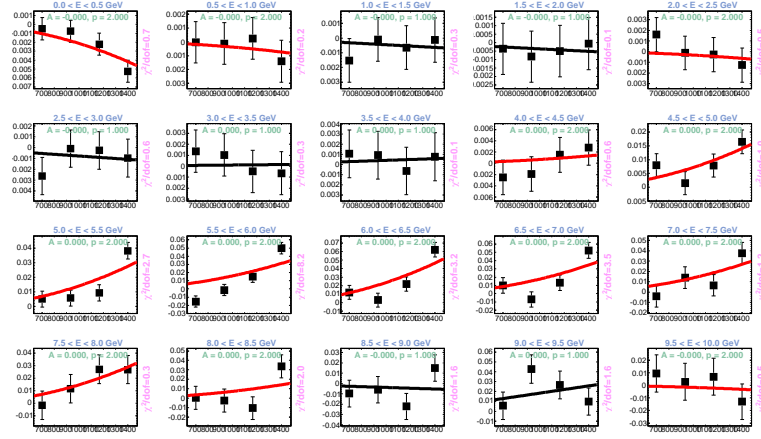


Figure 57: Fits to the near/far ratios for several values of **beam tilt in x** . Black(Red) fit lines indicate that a linear(parabolic) fit provided the best χ^2 .

A.12 Near Detector Position

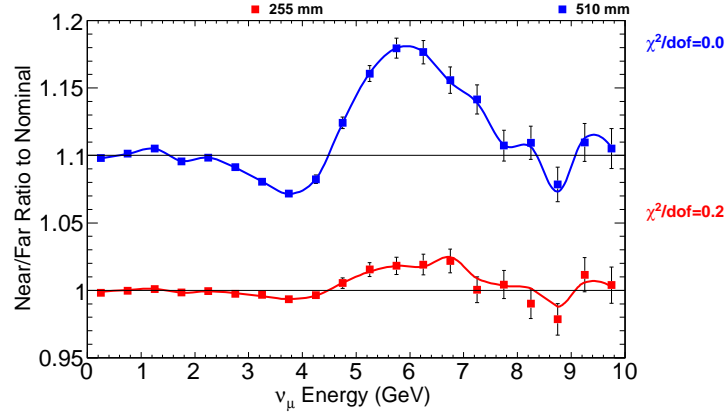


Figure 58: Near/Far double ratios to nominal for several values of **Near detector offset in x** (points) and the results of the fits to each energy bin (lines).

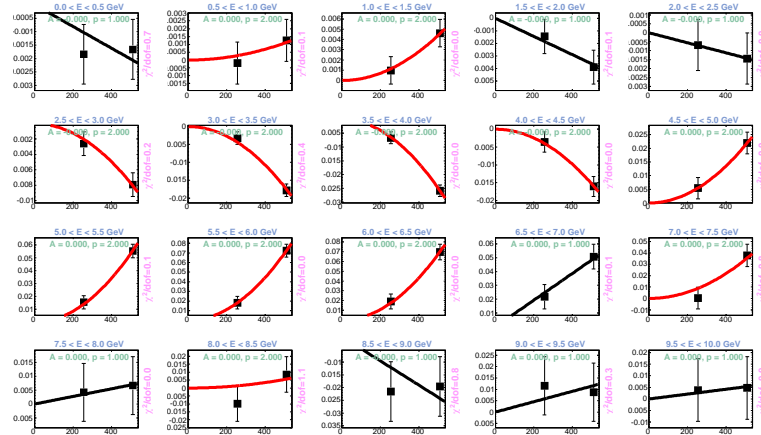


Figure 59: Fits to the near/far ratios for several values of **Near detector offset in x** . Black(Red) fit lines indicate that a linear(parabolic) fit provided the best χ^2 .

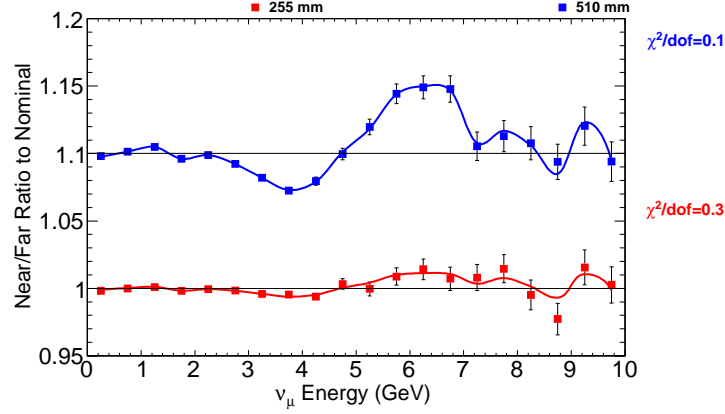


Figure 60: Near/Far double ratios to nominal for several values of **Near detector offset in y** (points) and the results of the fits to each energy bin (lines).

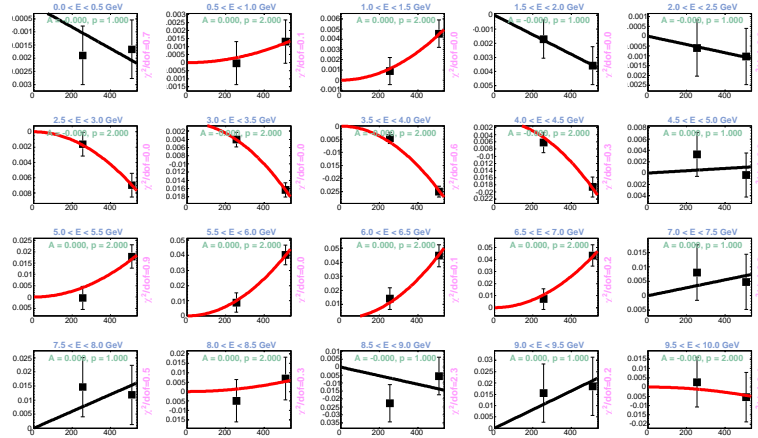


Figure 61: Fits to the near/far ratios for several values of **Near detector offset in y** . Black(Red) fit lines indicate that a linear(parabolic) fit provided the best χ^2 .

A.13 Horn Conductor Skin Depth

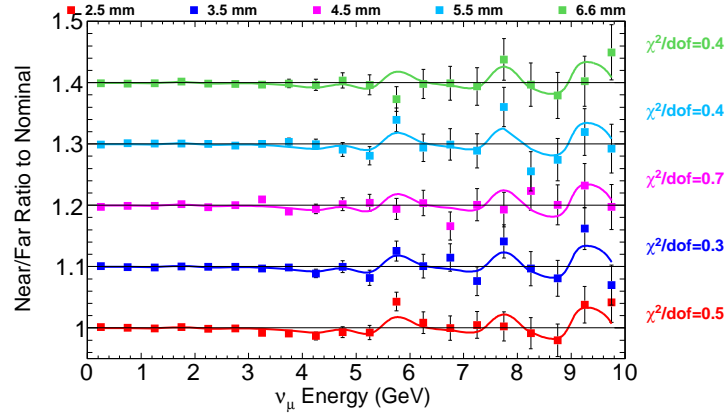


Figure 62: Near/Far double ratios to nominal for several values of **skin depth in the horn conductors** (points) and the results of the fits to each energy bin (lines).

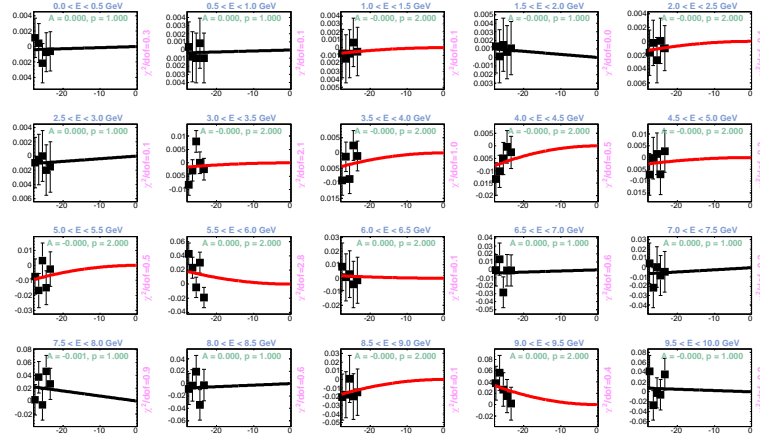


Figure 63: Fits to the near/far ratios for several values of **skin depth in the horn conductors**. Black(Red) fit lines indicate that a linear(parabolic) fit provided the best χ^2 .

B Near Detector Flux Ratios and Fits

B.1 Target Position

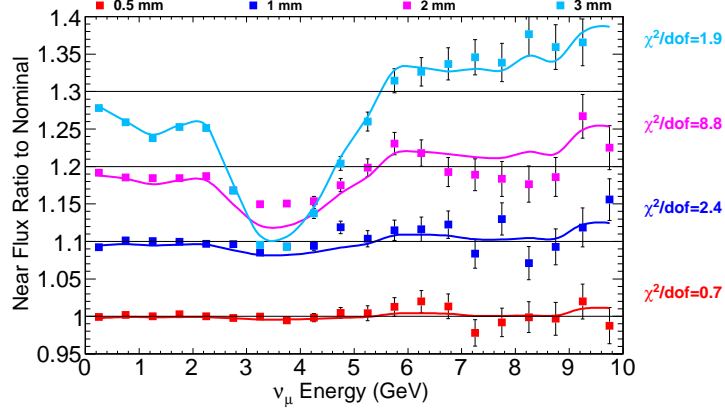


Figure 64: Near detector flux ratio to nominal for several values of **Target Offset in x** (points) and the results of the fits to each energy bin (lines).

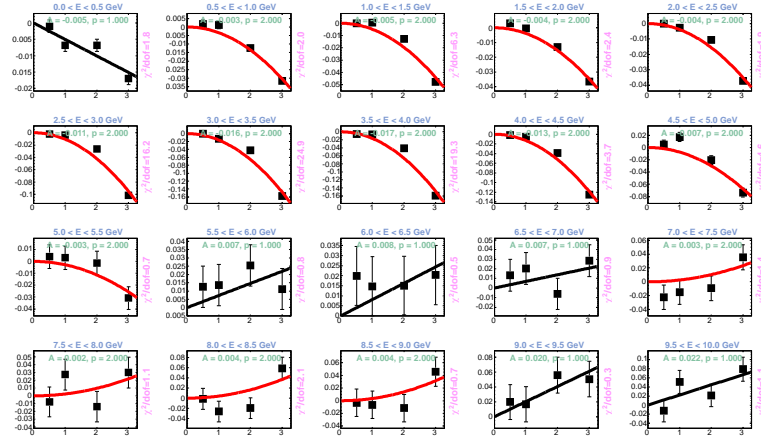


Figure 65: Fits to the near flux ratio for several values of **Target Offset in x** . Black(Red) fit lines indicate that a linear(parabolic) fit provided the best χ^2 .

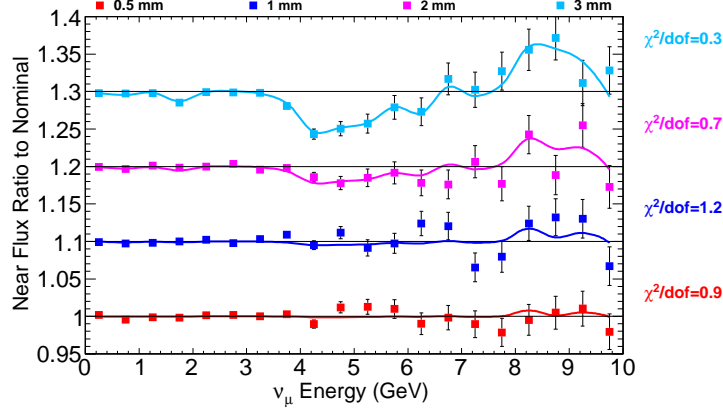


Figure 66: Near detector flux ratio to nominal for several values of **Target Offset in y** (points) and the results of the fits to each energy bin (lines).

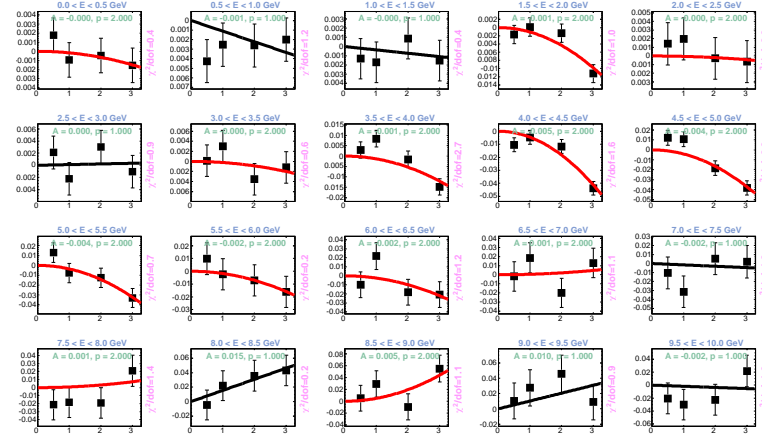


Figure 67: Fits to the near flux ratio for several values of **Target Offset in y** . Black(Red) fit lines indicate that a linear(parabolic) fit provided the best χ^2 .

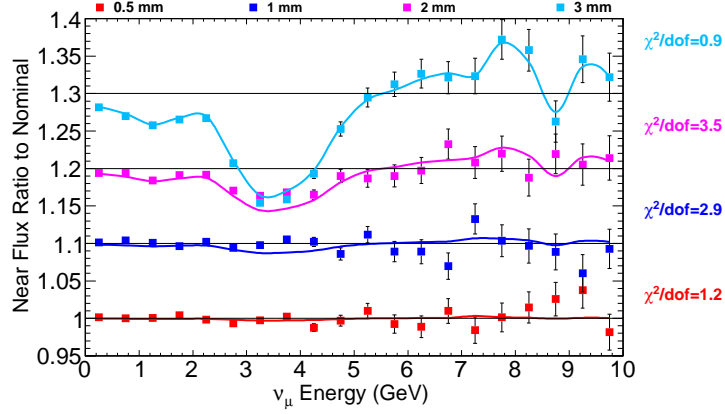


Figure 68: Near detector flux ratio to nominal for several values of **Target Tilt in x** (points) and the results of the fits to each energy bin (lines).

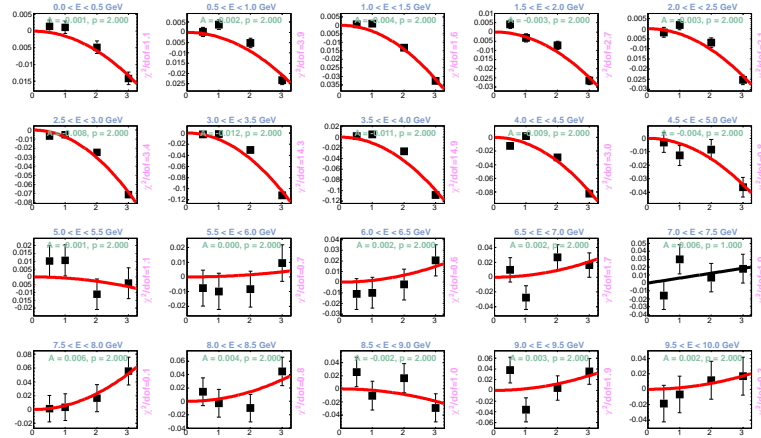


Figure 69: Fits to the near flux ratio for several values of **Target Tilt in x** . Black(Red) fit lines indicate that a linear(parabolic) fit provided the best χ^2 .

B.2 Horn 1 Position

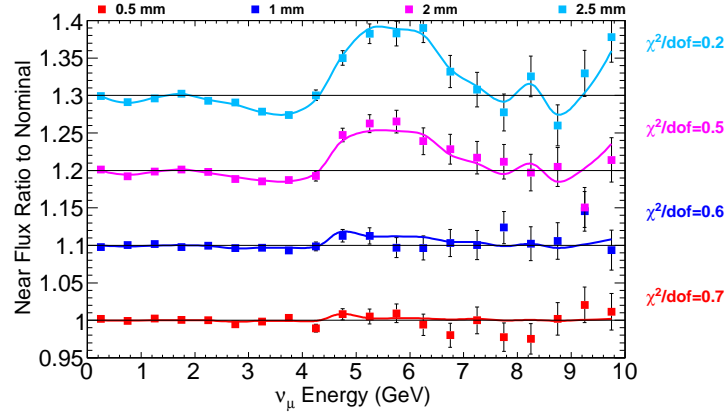


Figure 70: Near detector flux ratio to nominal for several values of **Horn 1 Offset in x** (points) and the results of the fits to each energy bin (lines).

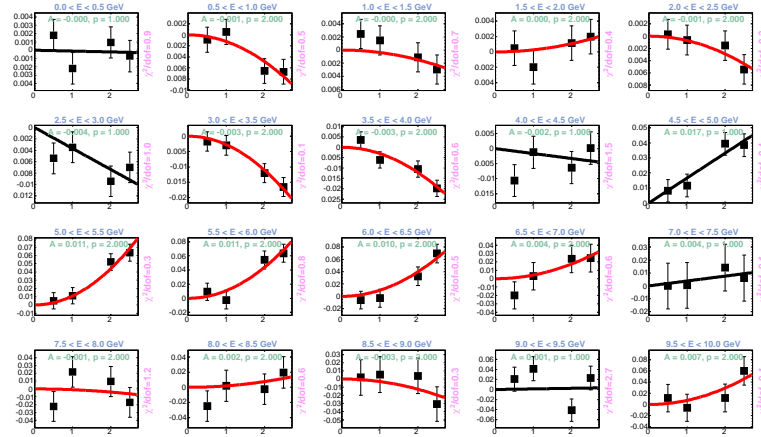


Figure 71: Fits to the near flux ratio for several values of **Horn 1 Offset in x** . Black(Red) fit lines indicate that a linear(parabolic) fit provided the best χ^2 .

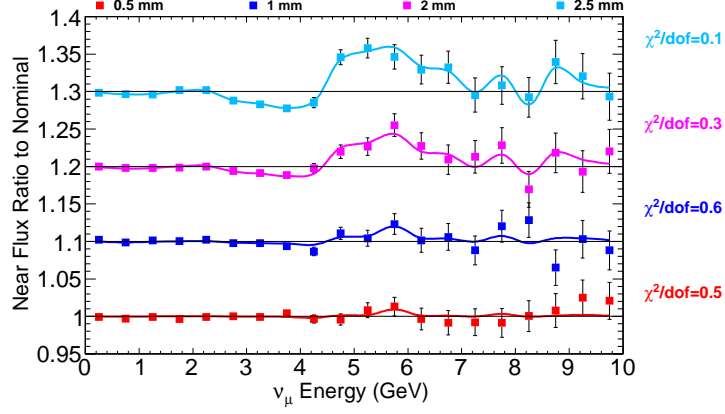


Figure 72: Near detector flux ratio to nominal for several values of **Horn 1 Offset** in y (points) and the results of the fits to each energy bin (lines).

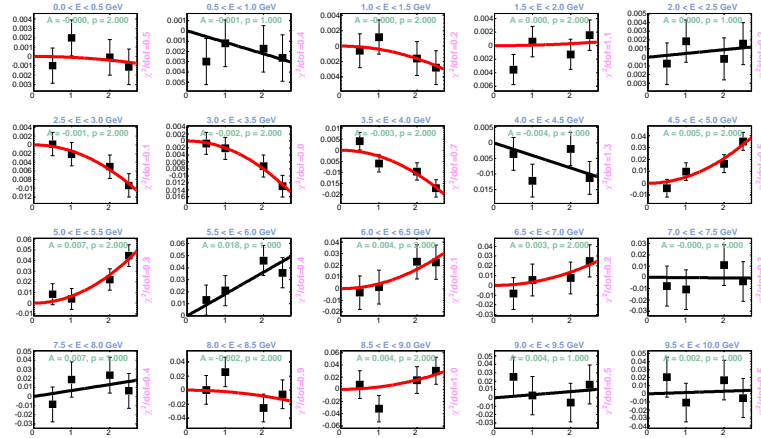


Figure 73: Fits to the near flux ratio for several values of **Horn 1 Offset** in y . Black(Red) fit lines indicate that a linear(parabolic) fit provided the best χ^2 .

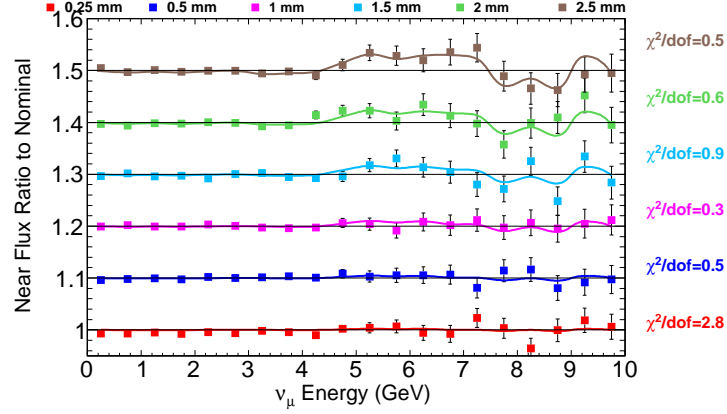


Figure 74: Near detector flux ratio to nominal for several values of **Horn 1 Tilt in x** (points) and the results of the fits to each energy bin (lines).

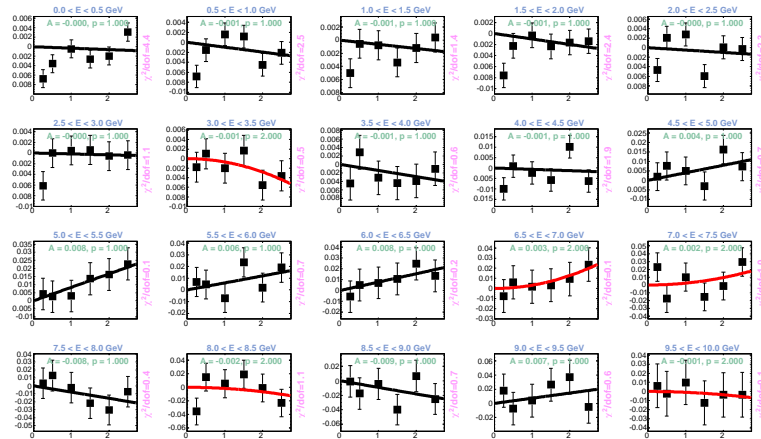


Figure 75: Fits to the near flux ratio for several values of **Horn 1 Tilt in x** . Black(Red) fit lines indicate that a linear(parabolic) fit provided the best χ^2 .

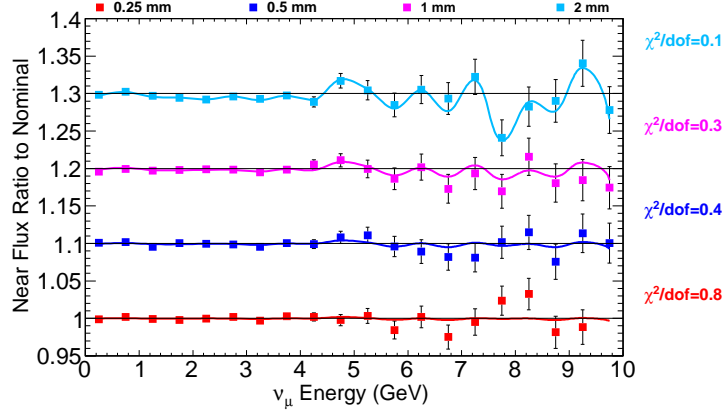


Figure 76: Near detector flux ratio to nominal for several values of **Horn 1 Tilt in y** (points) and the results of the fits to each energy bin (lines).

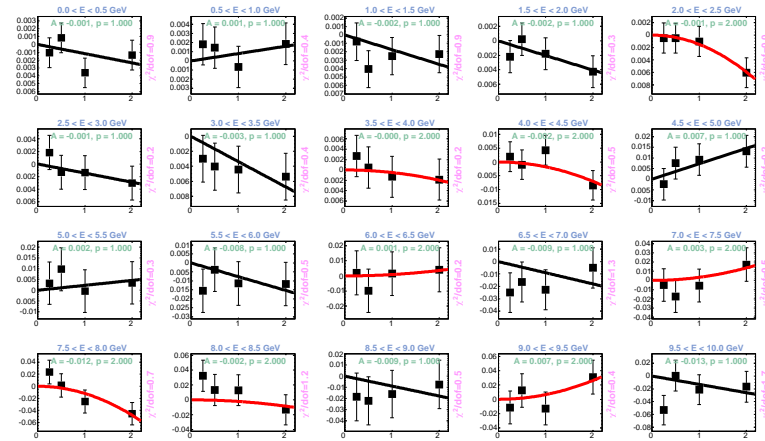


Figure 77: Fits to the near flux ratio for several values of **Horn 1 Tilt in y** . Black(Red) fit lines indicate that a linear(parabolic) fit provided the best χ^2 .

B.3 Horn 2 Position

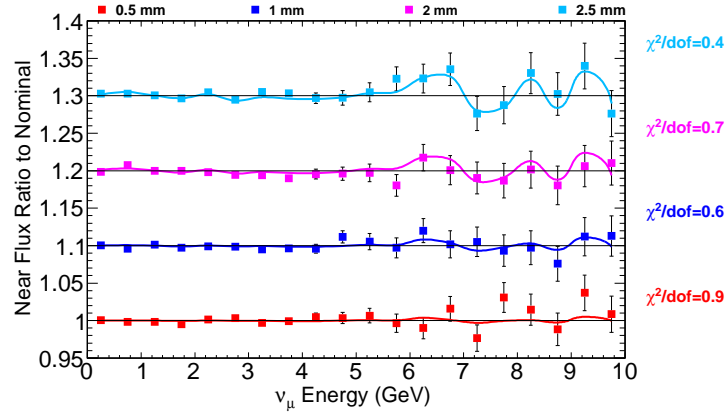


Figure 78: Near detector flux ratio to nominal for several values of **Horn 2 Offset in x** (points) and the results of the fits to each energy bin (lines).

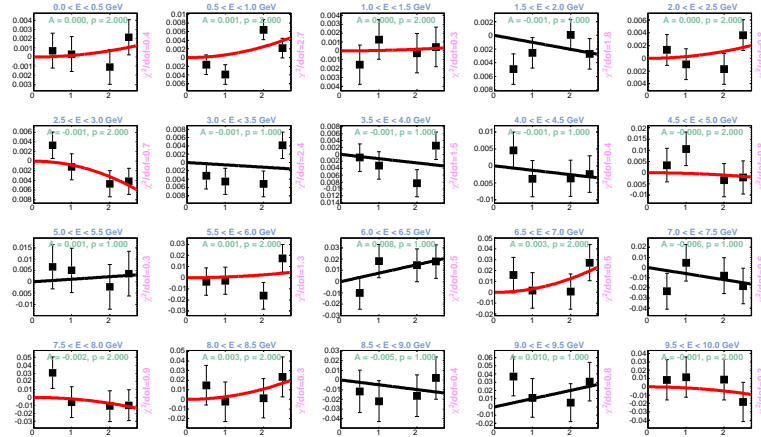


Figure 79: Fits to the near flux ratio for several values of **Horn 2 Offset in x** . Black(Red) fit lines indicate that a linear(parabolic) fit provided the best χ^2 .

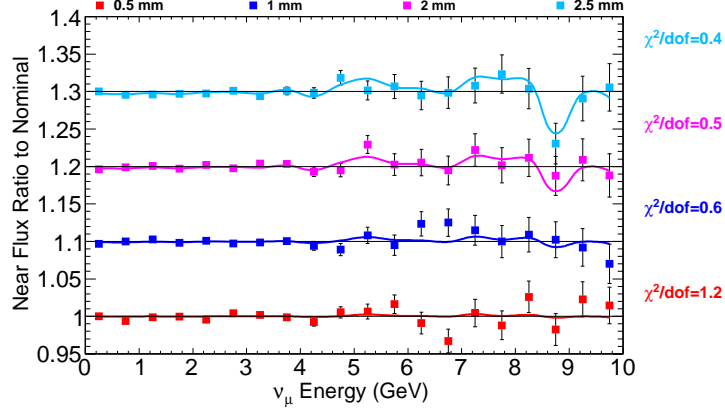


Figure 80: Near detector flux ratio to nominal for several values of **Horn 2 Offset** in y (points) and the results of the fits to each energy bin (lines).

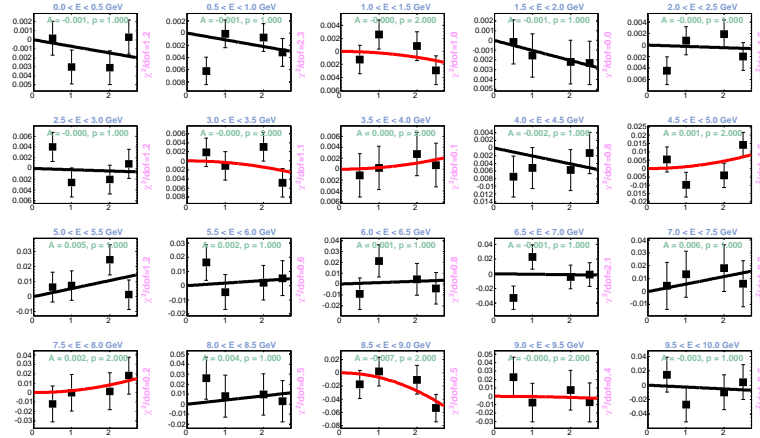


Figure 81: Fits to the near flux ratio for several values of **Horn 2 Offset** in y . Black(Red) fit lines indicate that a linear(parabolic) fit provided the best χ^2 .

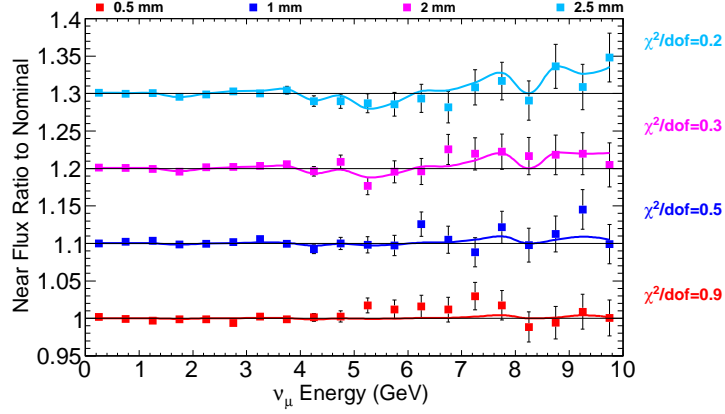


Figure 82: Near detector flux ratio to nominal for several values of **Horn 2 Tilt in x** (points) and the results of the fits to each energy bin (lines).

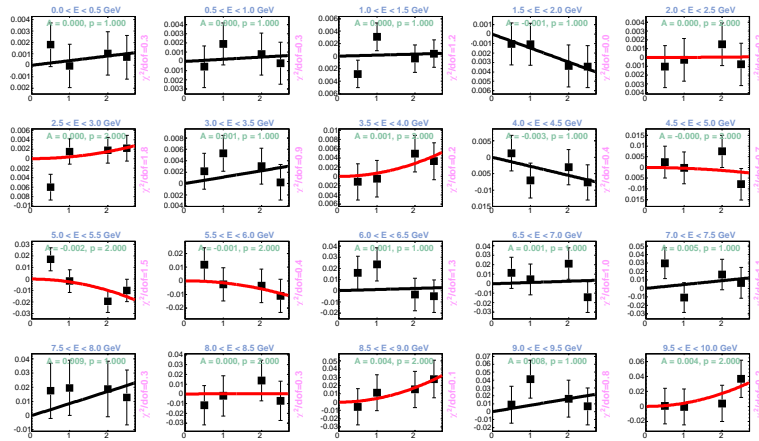


Figure 83: Fits to the near flux ratio for several values of **Horn 2 Tilt in x** . Black(Red) fit lines indicate that a linear(parabolic) fit provided the best χ^2 .

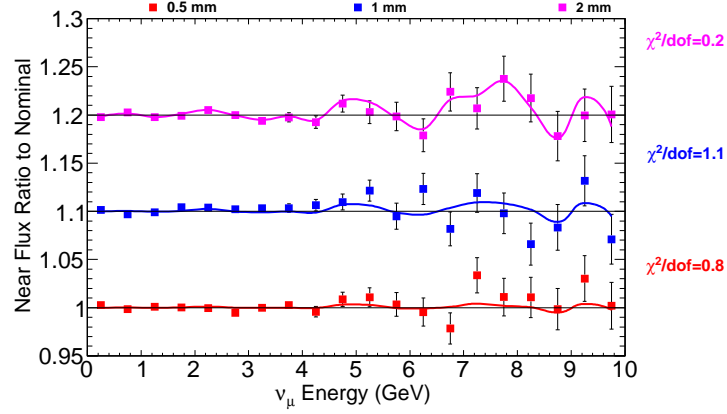


Figure 84: Near detector flux ratio to nominal for several values of **Horn 2 Tilt in y** (points) and the results of the fits to each energy bin (lines).

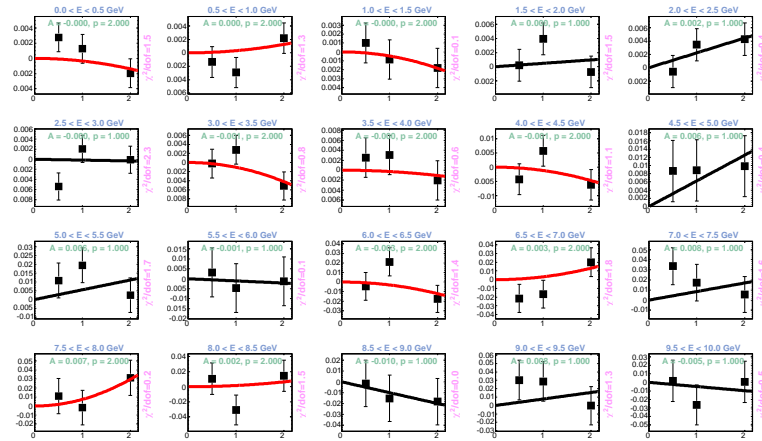


Figure 85: Fits to the near flux ratio for several values of **Horn 2 Tilt in y** . Black(Red) fit lines indicate that a linear(parabolic) fit provided the best χ^2 .

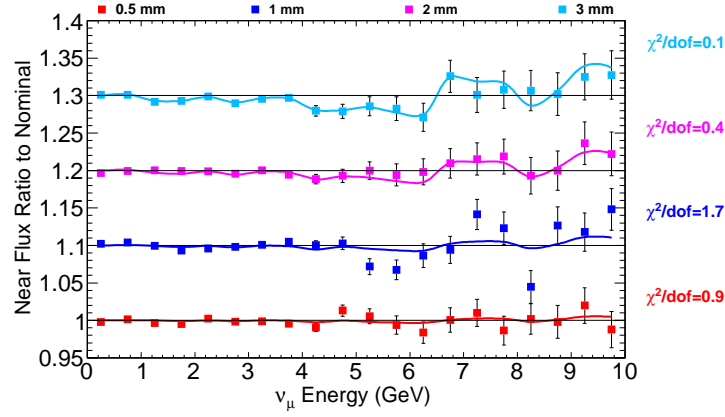


Figure 86: Near detector flux ratio to nominal for several values of **Target Tilt in y** (points) and the results of the fits to each energy bin (lines).

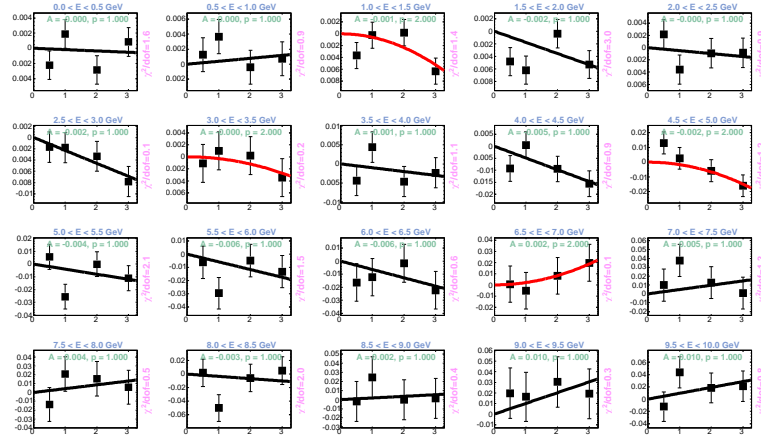


Figure 87: Fits to the near flux ratio for several values of **Target Tilt in y** . Black(Red) fit lines indicate that a linear(parabolic) fit provided the best χ^2 .

B.4 Far Detector Position

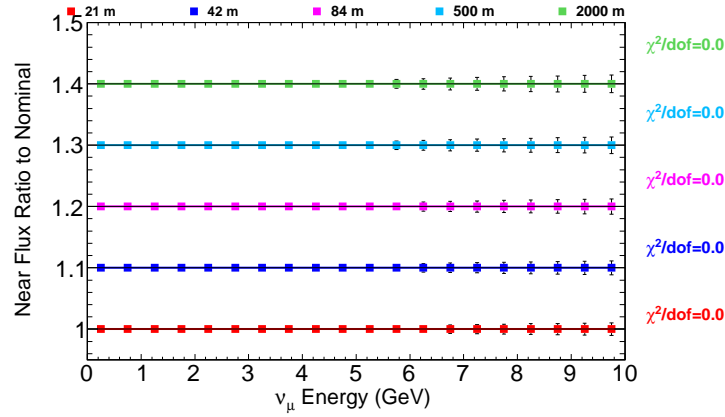


Figure 88: Near detector flux ratio to nominal for several values of **Far detector offset in x** (points) and the results of the fits to each energy bin (lines).

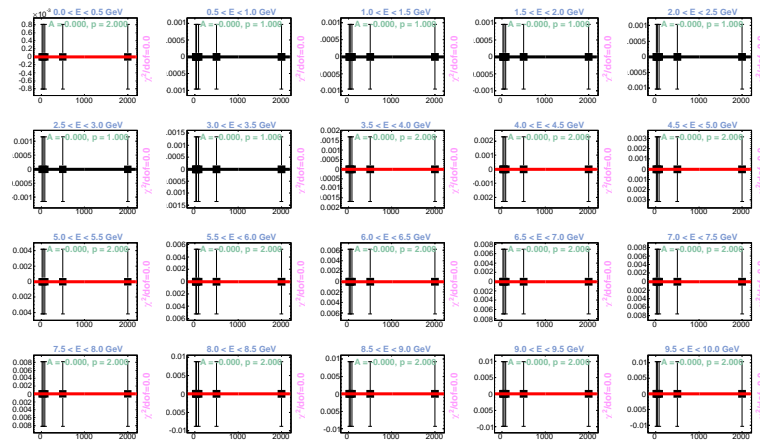


Figure 89: Fits to the near flux ratio for several values of **Far detector offset in x** . Black(Red) fit lines indicate that a linear(parabolic) fit provided the best χ^2 .

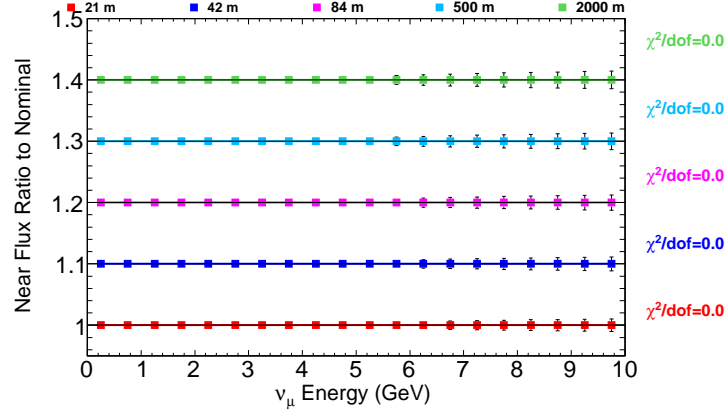


Figure 90: Near detector flux ratio to nominal for several values of **Far detector offset in y** (points) and the results of the fits to each energy bin (lines).

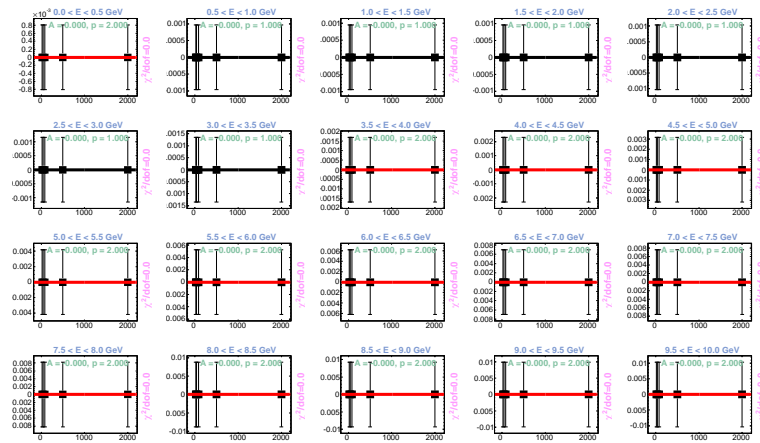


Figure 91: Fits to the near flux ratio for several values of **Far detector offset in y** . Black(Red) fit lines indicate that a linear(parabolic) fit provided the best χ^2 .

B.5 Decay Pipe Position

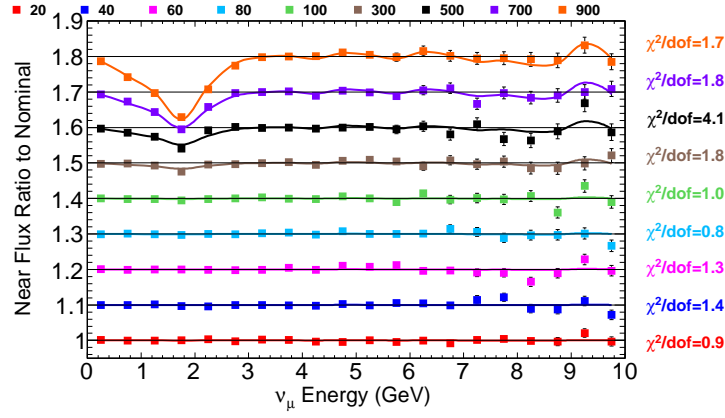


Figure 92: Near detector flux ratio to nominal for several values of **Decay Pipe Offset in x** (points) and the results of the fits to each energy bin (lines).

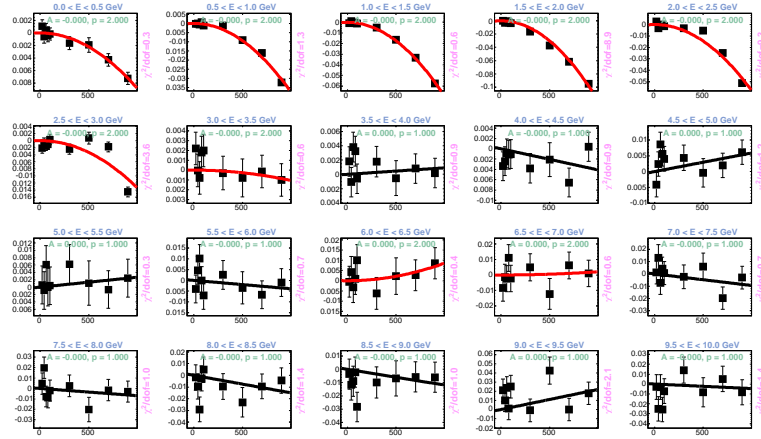


Figure 93: Fits to the near flux ratio for several values of **Decay Pipe Offset in x** . Black(Red) fit lines indicate that a linear(parabolic) fit provided the best χ^2 .

B.6 Decay Pipe Radius

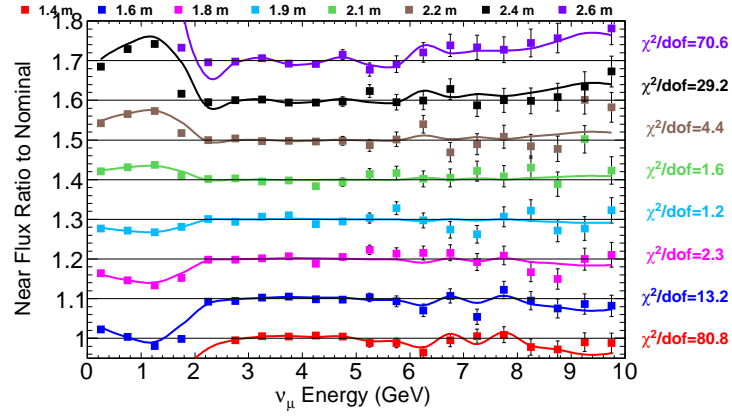


Figure 94: Near detector flux ratio to nominal for several values of **Decay Pipe Radius** (points) and the results of the fits to each energy bin (lines).

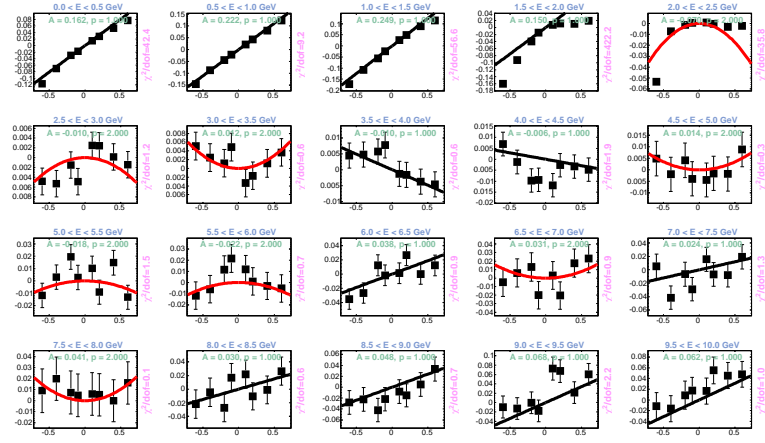


Figure 95: Fits to the near flux ratio for several values of **Decay Pipe Radius**. Black(Red) fit lines indicate that a linear(parabolic) fit provided the best χ^2 .

B.7 Horn Current

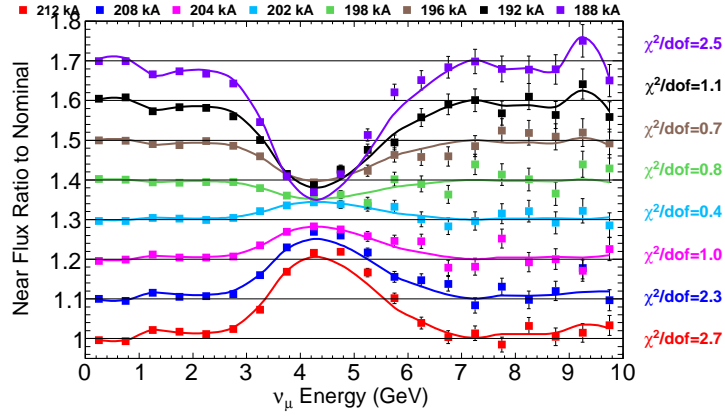


Figure 96: Near detector flux ratio to nominal for several values of **Horn Current** (points) and the results of the fits to each energy bin (lines).

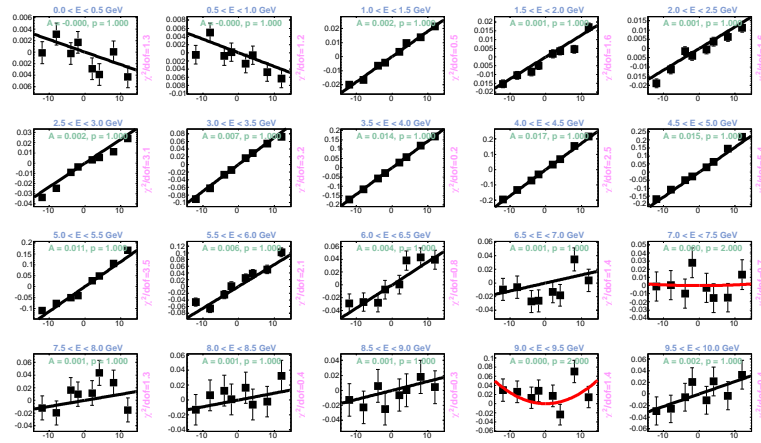


Figure 97: Fits to the near flux ratio for several values of **Horn Current**. Black(Red) fit lines indicate that a linear(parabolic) fit provided the best χ^2 .

B.8 Horn Water Layer Thickness

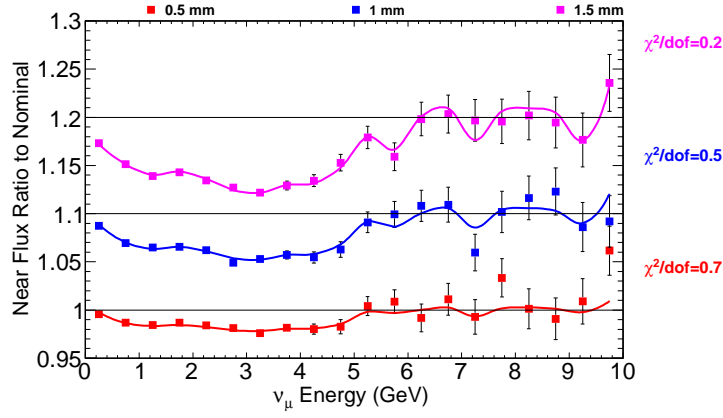


Figure 98: Near detector flux ratio to nominal for several values of **horn cooling water layer thickness** (points) and the results of the fits to each energy bin (lines).

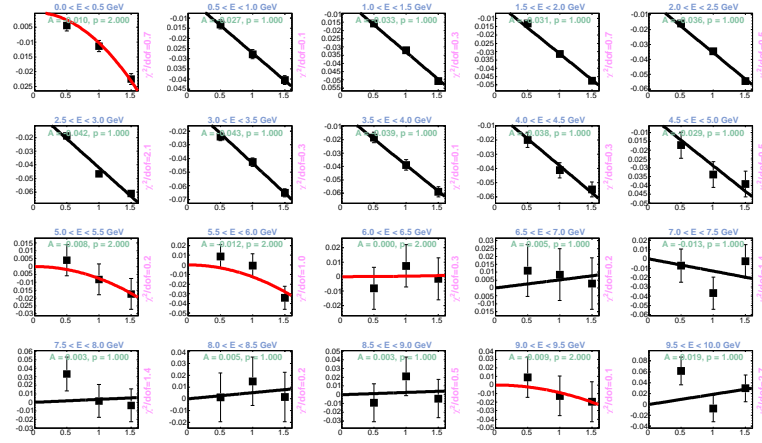


Figure 99: Fits to the near flux ratio for several values of **horn cooling water layer thickness**. Black(Red) fit lines indicate that a linear(parabolic) fit provided the best χ^2 .

B.9 Beam size at target

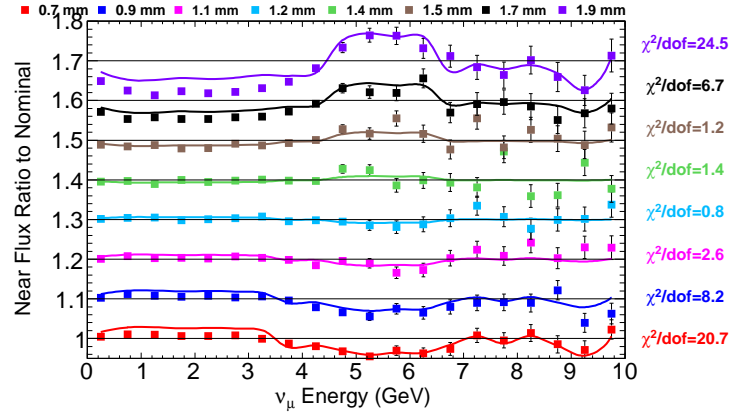


Figure 100: Near detector flux ratio to nominal for several values of **Beam size in x** (points) and the results of the fits to each energy bin (lines).

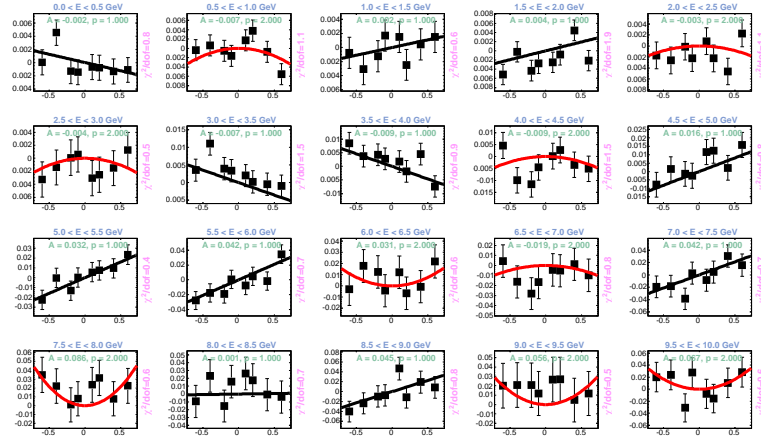


Figure 101: Fits to the near flux ratio for several values of **Beam size in x** . Black(Red) fit lines indicate that a linear(parabolic) fit provided the best χ^2 .

B.10 Beam Position at Target

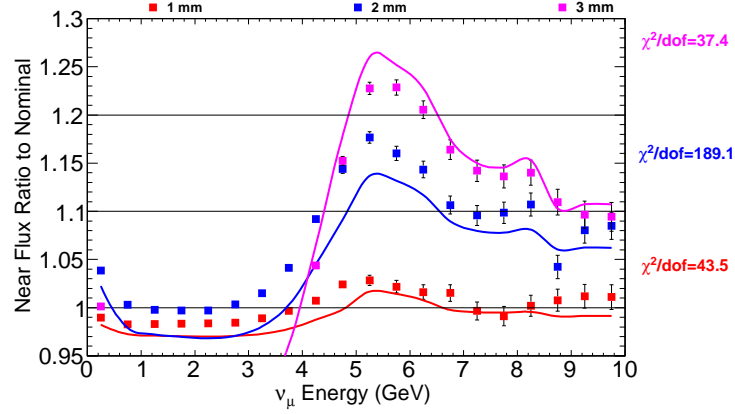


Figure 102: Near detector flux ratio to nominal for several values of **Beam x offset at target** (points) and the results of the fits to each energy bin (lines).

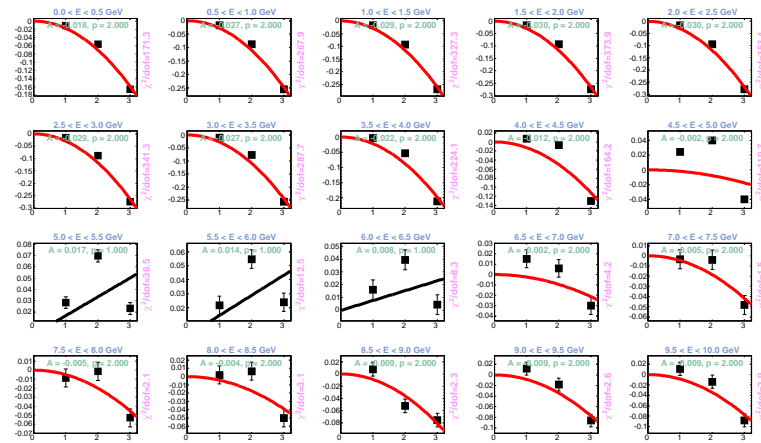


Figure 103: Fits to the near flux ratio for several values of **Beam x offset at target**. Black(Red) fit lines indicate that a linear(parabolic) fit provided the best χ^2 .

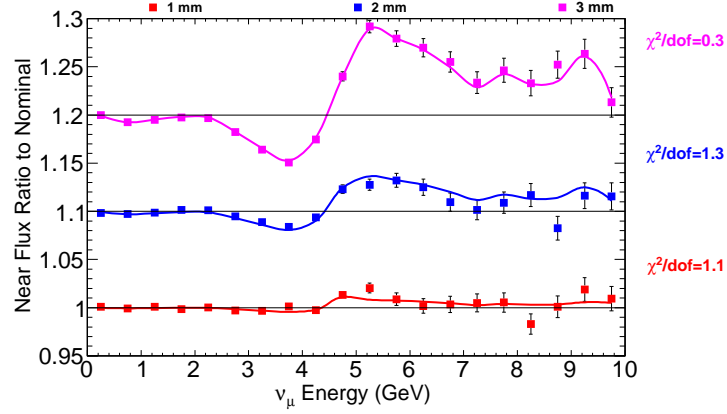


Figure 104: Near detector flux ratio to nominal for several values of **Beam y offset at target** (points) and the results of the fits to each energy bin (lines).

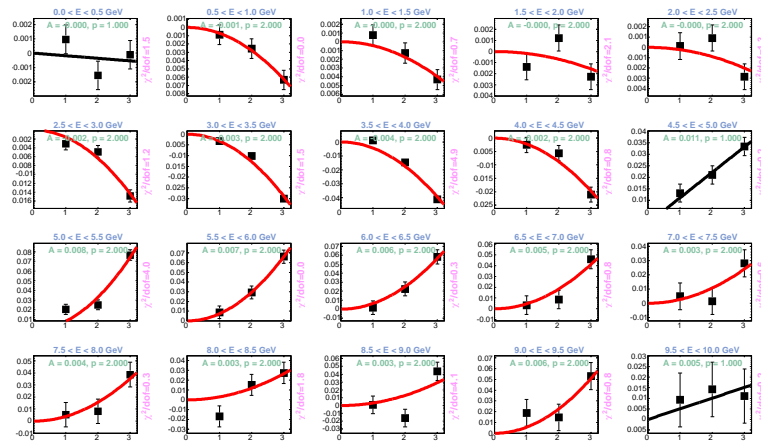


Figure 105: Fits to the near flux ratio for several values of **Beam y offset at target**. Black(Red) fit lines indicate that a linear(parabolic) fit provided the best χ^2 .

B.11 Beam Angle at Target

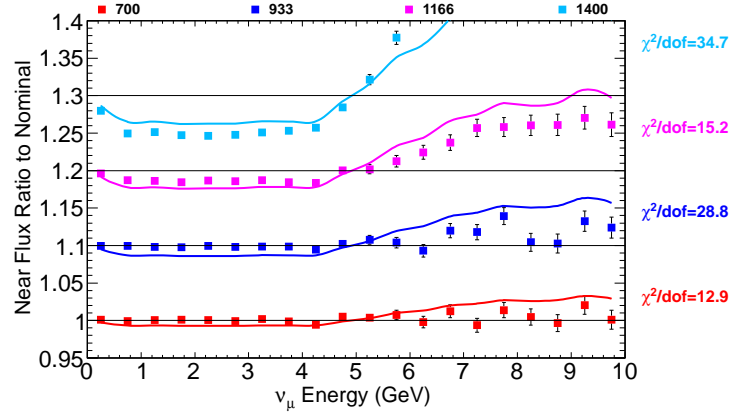


Figure 106: Near detector flux ratio to nominal for several values of **beam tilt in x** (points) and the results of the fits to each energy bin (lines).

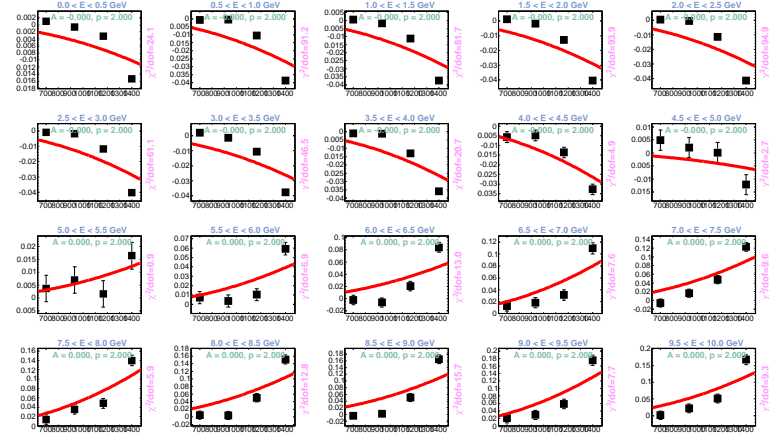


Figure 107: Fits to the near flux ratio for several values of **beam tilt in x** . Black(Red) fit lines indicate that a linear(parabolic) fit provided the best χ^2 .

B.12 Near Detector Position

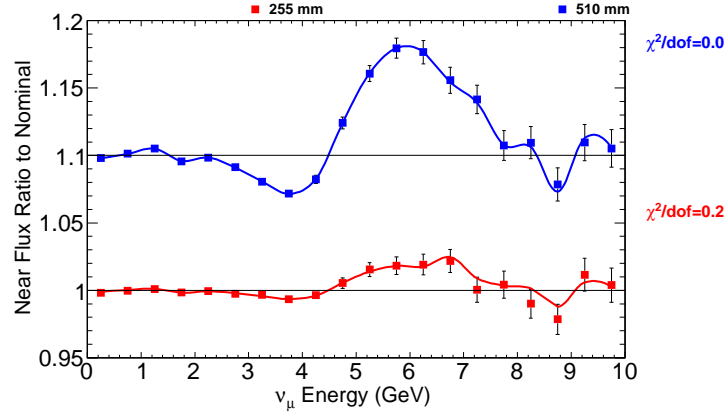


Figure 108: Near detector flux ratio to nominal for several values of **Near detector offset in x** (points) and the results of the fits to each energy bin (lines).

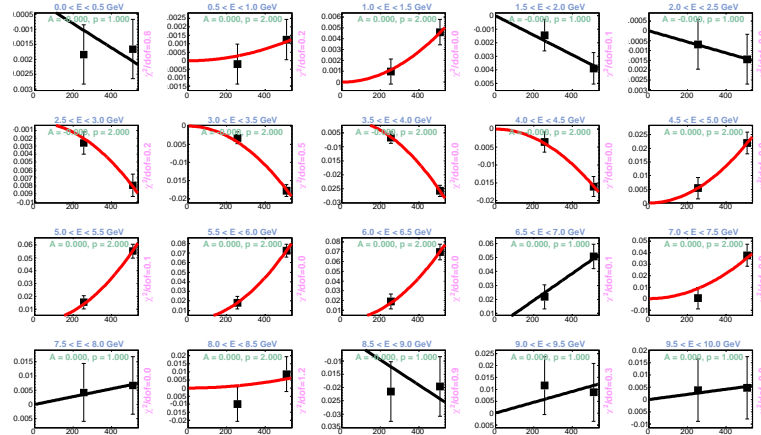


Figure 109: Fits to the near flux ratio for several values of **Near detector offset in x** . Black(Red) fit lines indicate that a linear(parabolic) fit provided the best χ^2 .

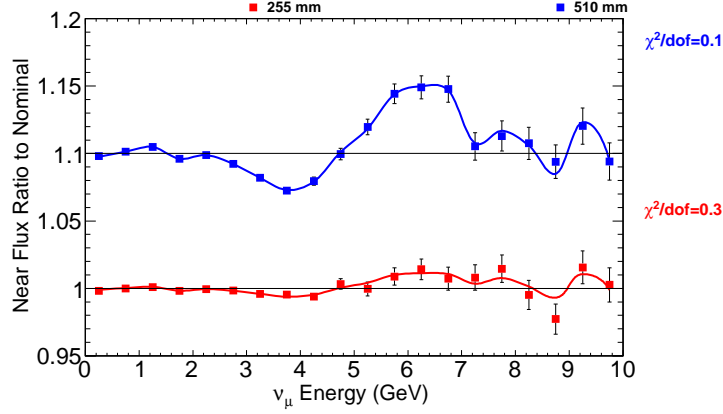


Figure 110: Near detector flux ratio to nominal for several values of **Near detector offset in y** (points) and the results of the fits to each energy bin (lines).

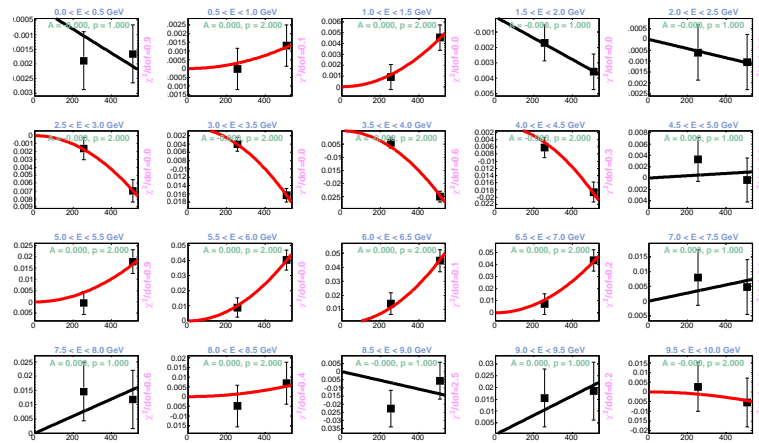


Figure 111: Fits to the near flux ratio for several values of **Near detector offset in y** . Black(Red) fit lines indicate that a linear(parabolic) fit provided the best χ^2 .

B.13 Horn Conductor Skin Depth

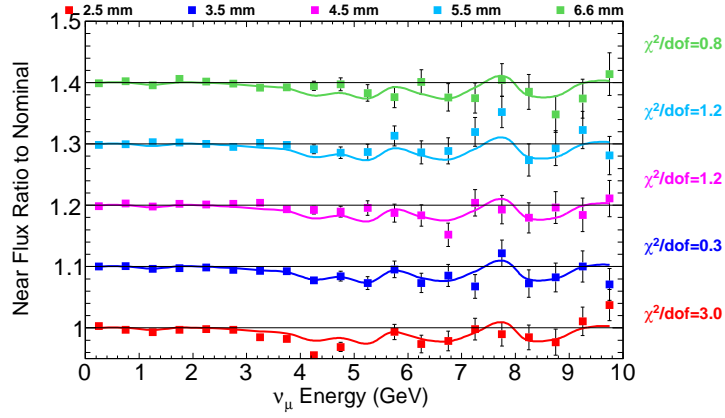


Figure 112: Near detector flux ratio to nominal for several values of **skin depth in the horn conductors** (points) and the results of the fits to each energy bin (lines).

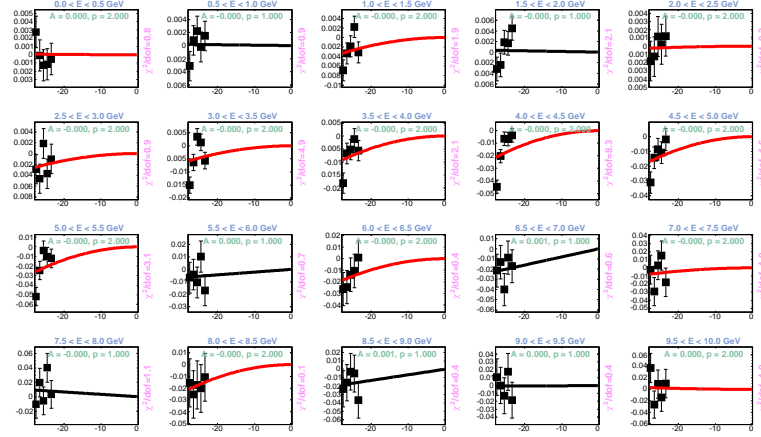


Figure 113: Fits to the near flux ratio for several values of **skin depth in the horn conductors**. Black(Red) fit lines indicate that a linear(parabolic) fit provided the best χ^2 .

C Gar Detector Flux Ratios and Fits

C.1 Target Position

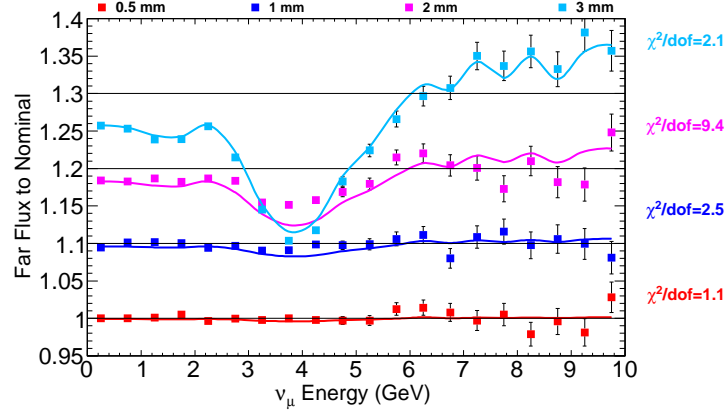


Figure 114: Far detector flux ratio to nominal for several values of **Target Offset in x** (points) and the results of the fits to each energy bin (lines).

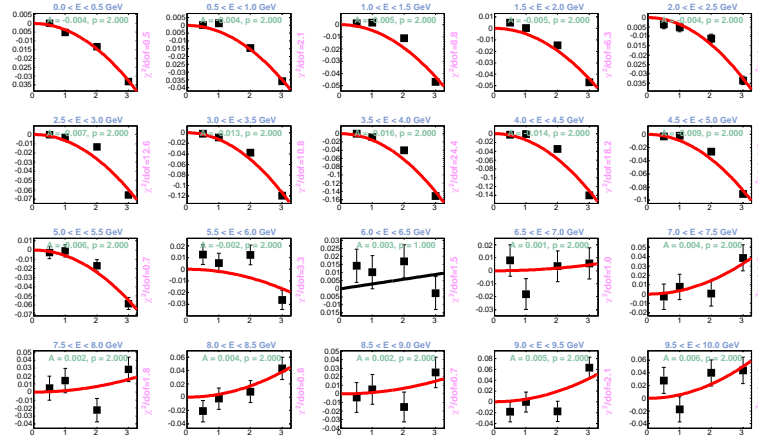


Figure 115: Fits to the far flux ratio for several values of **Target Offset in x** . Black(Red) fit lines indicate that a linear(parabolic) fit provided the best χ^2 .

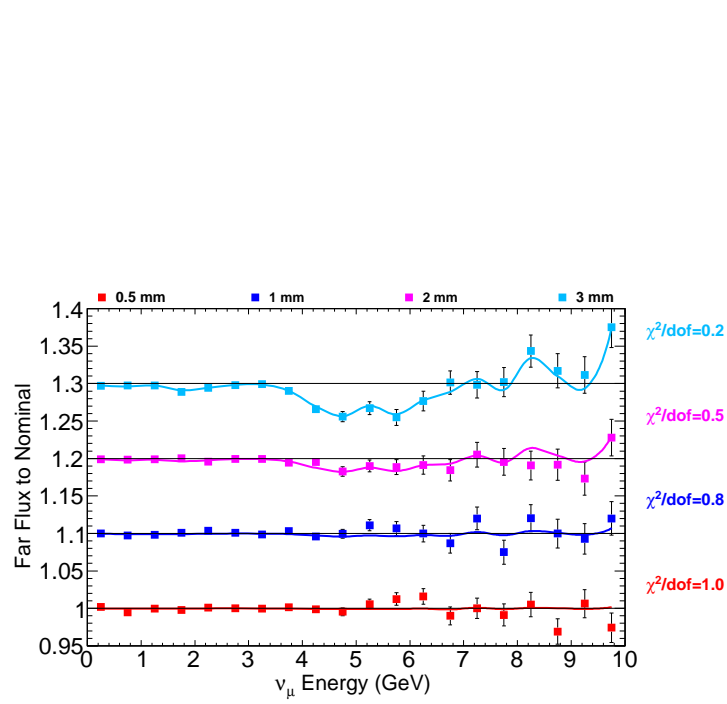


Figure 116: Far detector flux ratio to nominal for several values of **Target Offset in y** (points) and the results of the fits to each energy bin (lines).

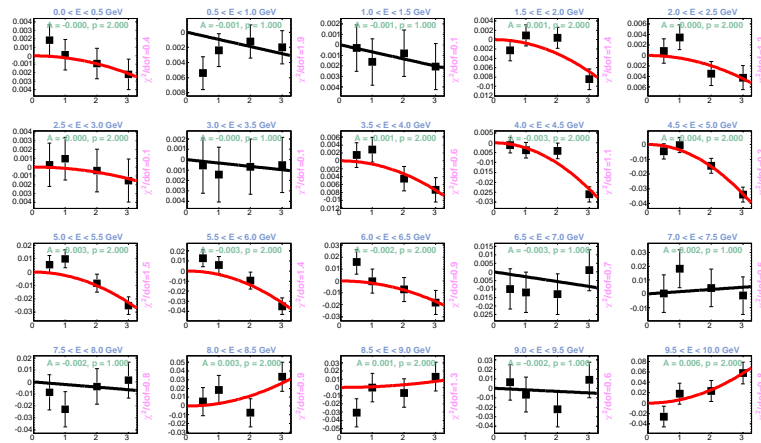


Figure 117: Fits to the far flux ratio for several values of **Target Offset in y** . Black(Red) fit lines indicate that a linear(parabolic) fit provided the best χ^2 .

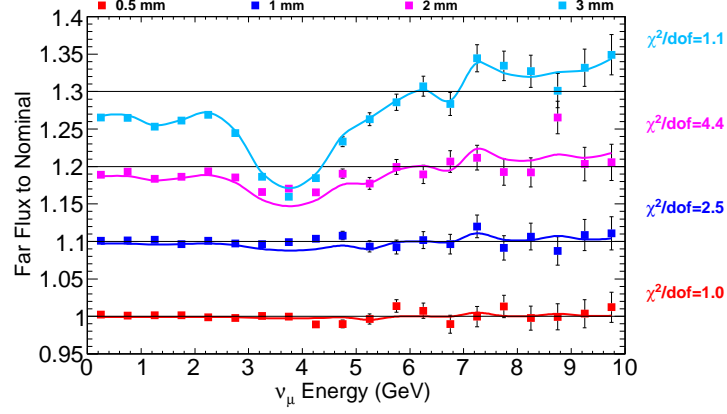


Figure 118: Far detector flux ratio to nominal for several values of **Target Tilt in x** (points) and the results of the fits to each energy bin (lines).

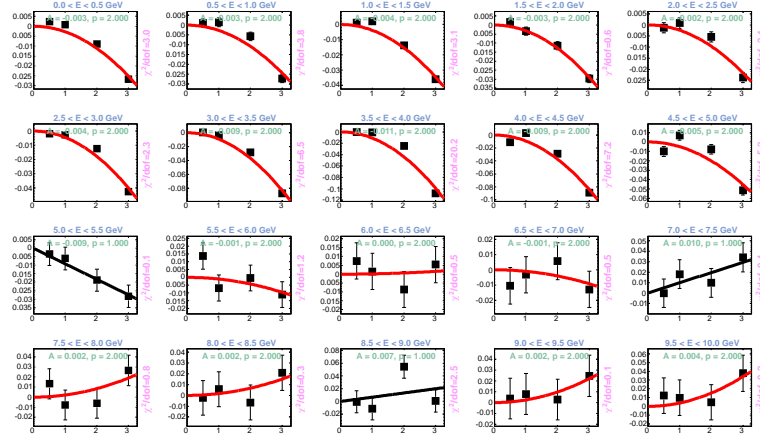


Figure 119: Fits to the far flux ratio for several values of **Target Tilt in x** . Black(Red) fit lines indicate that a linear(parabolic) fit provided the best χ^2 .

C.2 Horn 1 Position

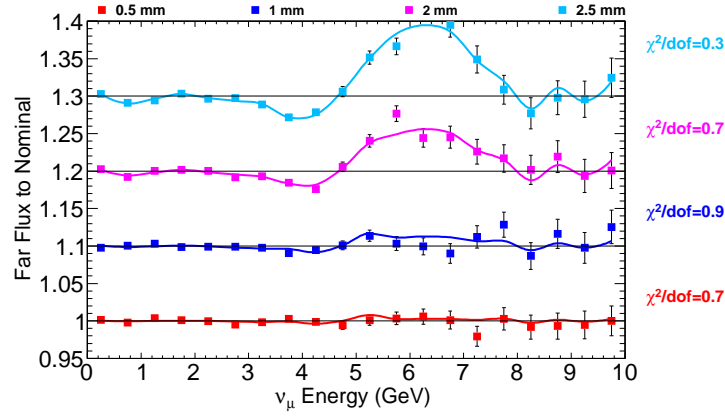


Figure 120: Far detector flux ratio to nominal for several values of **Horn 1 Offset in x** (points) and the results of the fits to each energy bin (lines).

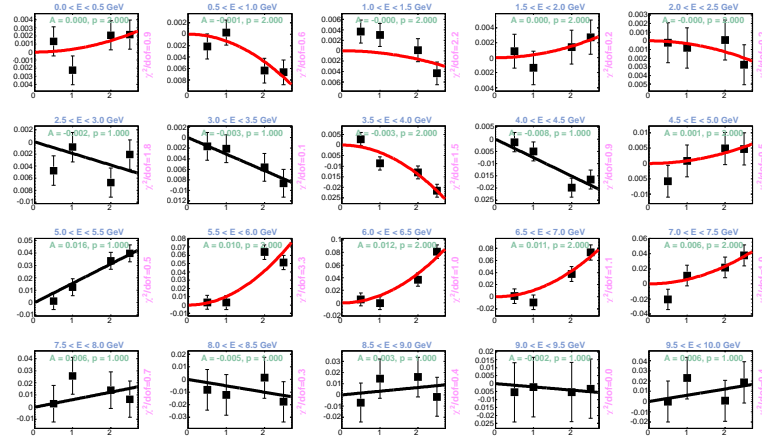


Figure 121: Fits to the far flux ratio for several values of **Horn 1 Offset in x** . Black(Red) fit lines indicate that a linear(parabolic) fit provided the best χ^2 .

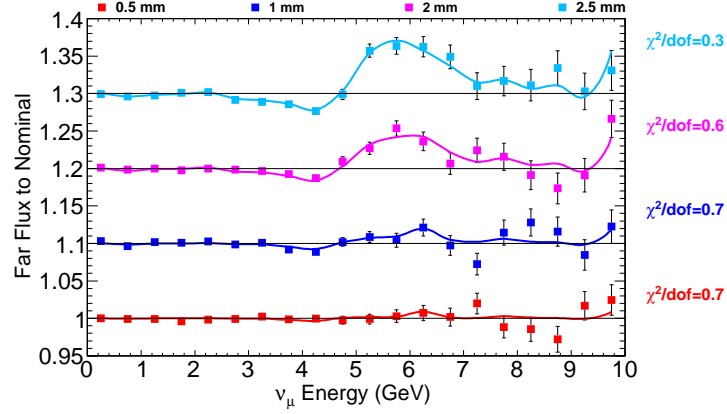


Figure 122: Far detector flux ratio to nominal for several values of **Horn 1 Offset in y** (points) and the results of the fits to each energy bin (lines).

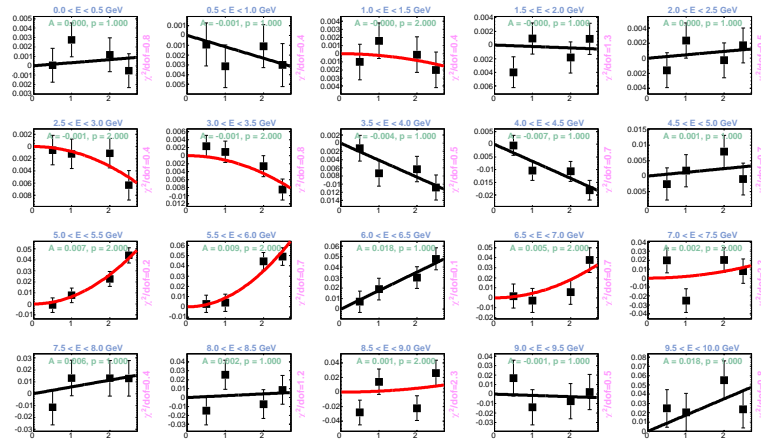


Figure 123: Fits to the far flux ratio for several values of **Horn 1 Offset in y** . Black(Red) fit lines indicate that a linear(parabolic) fit provided the best χ^2 .

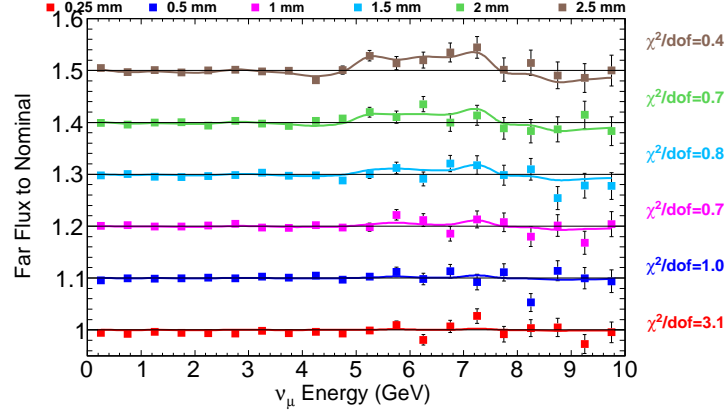


Figure 124: Far detector flux ratio to nominal for several values of **Horn 1 Tilt in x** (points) and the results of the fits to each energy bin (lines).

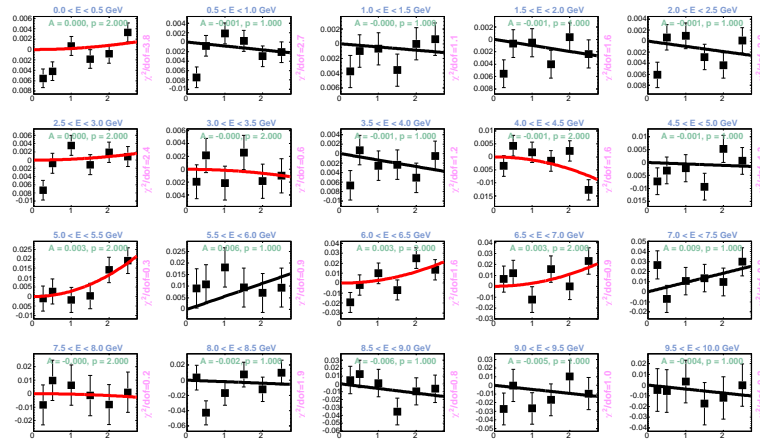


Figure 125: Fits to the far flux ratio for several values of **Horn 1 Tilt in x** . Black(Red) fit lines indicate that a linear(parabolic) fit provided the best χ^2 .

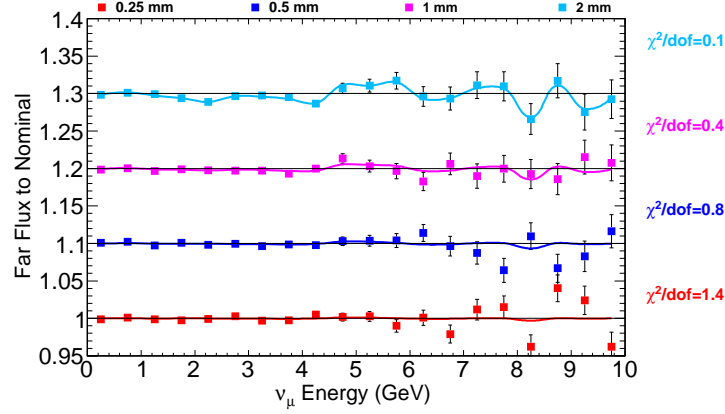


Figure 126: Far detector flux ratio to nominal for several values of **Horn 1 Tilt in y** (points) and the results of the fits to each energy bin (lines).

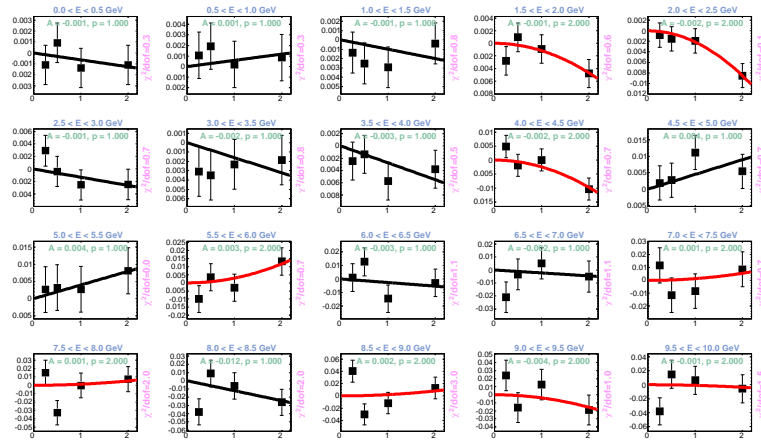


Figure 127: Fits to the far flux ratio for several values of **Horn 1 Tilt in y** . Black(Red) fit lines indicate that a linear(parabolic) fit provided the best χ^2 .

C.3 Horn 2 Position

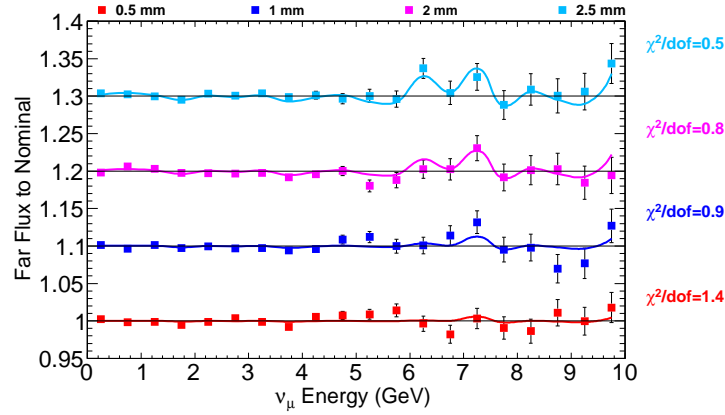


Figure 128: Far detector flux ratio to nominal for several values of **Horn 2 Offset in x** (points) and the results of the fits to each energy bin (lines).

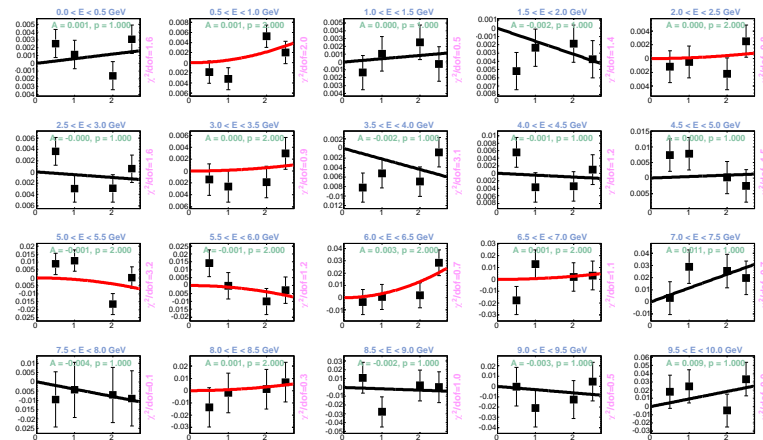


Figure 129: Fits to the far flux ratio for several values of **Horn 2 Offset in x** . Black(Red) fit lines indicate that a linear(parabolic) fit provided the best χ^2 .

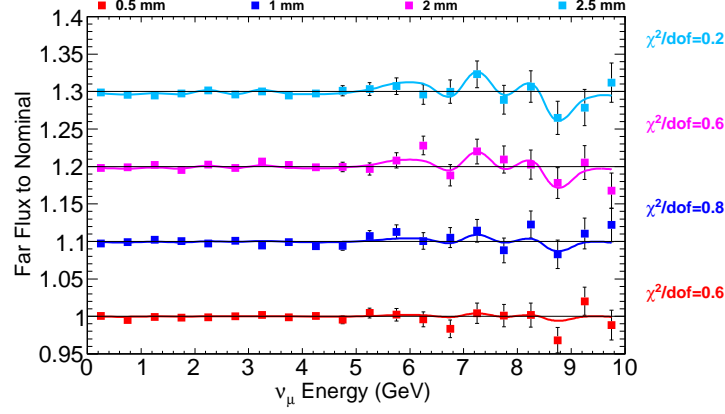


Figure 130: Far detector flux ratio to nominal for several values of **Horn 2 Offset in y** (points) and the results of the fits to each energy bin (lines).

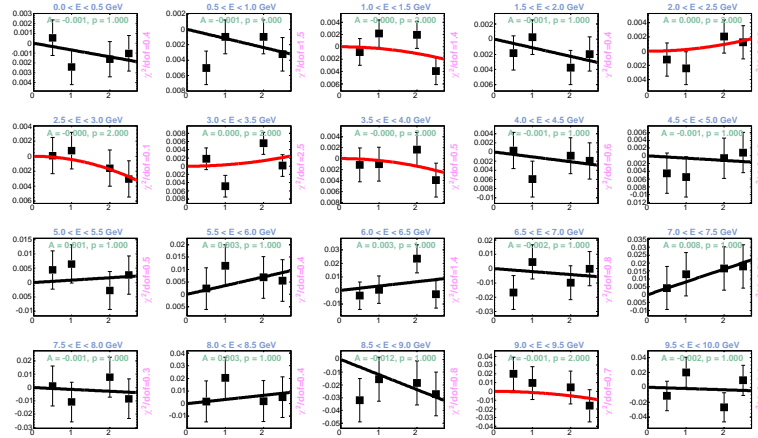


Figure 131: Fits to the far flux ratio for several values of **Horn 2 Offset in y** . Black(Red) fit lines indicate that a linear(parabolic) fit provided the best χ^2 .

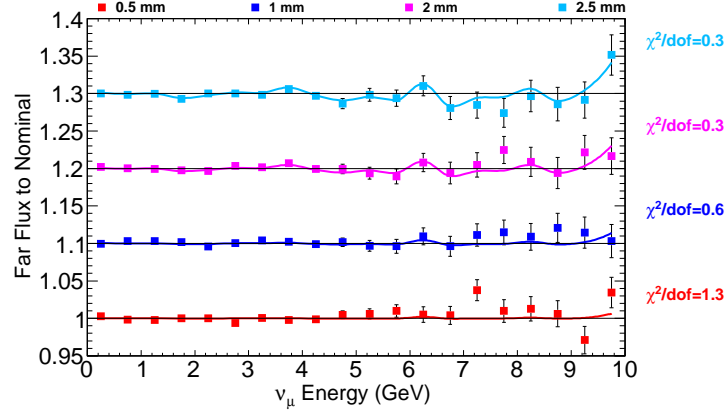


Figure 132: Far detector flux ratio to nominal for several values of **Horn 2 Tilt in x** (points) and the results of the fits to each energy bin (lines).

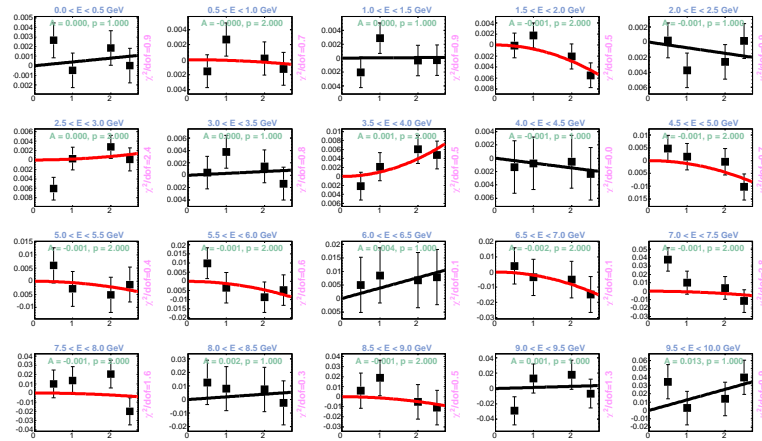


Figure 133: Fits to the far flux ratio for several values of **Horn 2 Tilt in x** . Black(Red) fit lines indicate that a linear(parabolic) fit provided the best χ^2 .

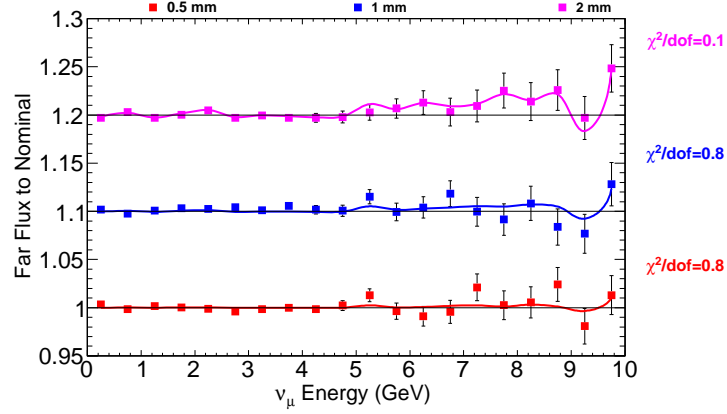


Figure 134: Far detector flux ratio to nominal for several values of **Horn 2 Tilt in y** (points) and the results of the fits to each energy bin (lines).

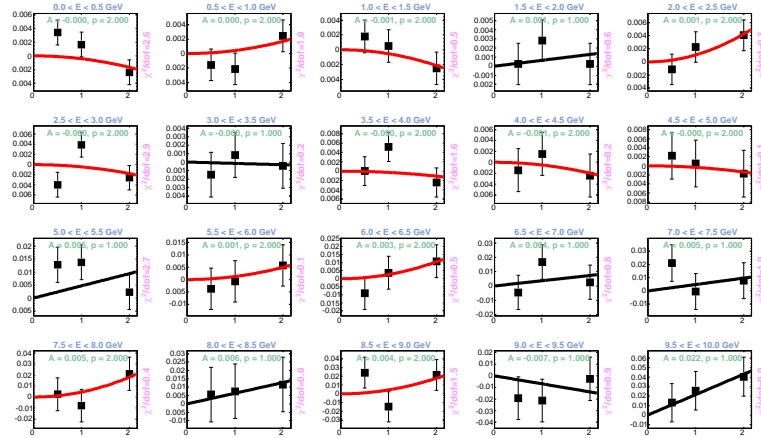


Figure 135: Fits to the far flux ratio for several values of **Horn 2 Tilt in y** . Black(Red) fit lines indicate that a linear(parabolic) fit provided the best χ^2 .

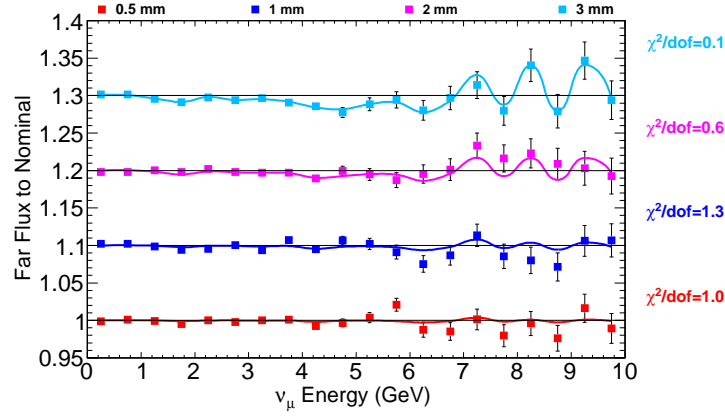


Figure 136: Far detector flux ratio to nominal for several values of **Target Tilt in y** (points) and the results of the fits to each energy bin (lines).

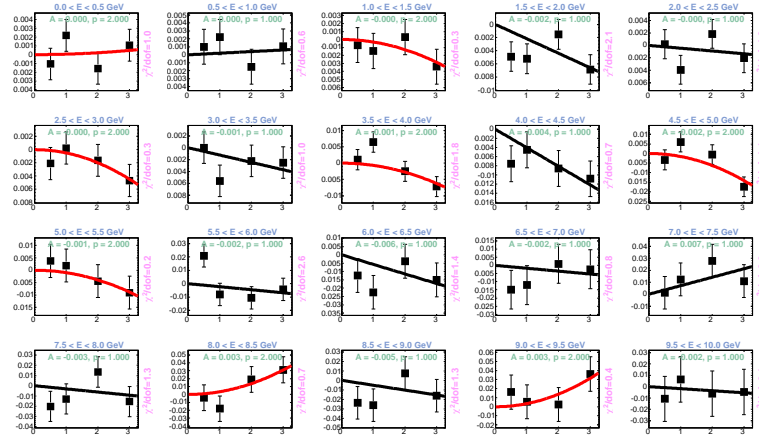


Figure 137: Fits to the far flux ratio for several values of **Target Tilt in y** . Black(Red) fit lines indicate that a linear(parabolic) fit provided the best χ^2 .

C.4 Far Detector Position

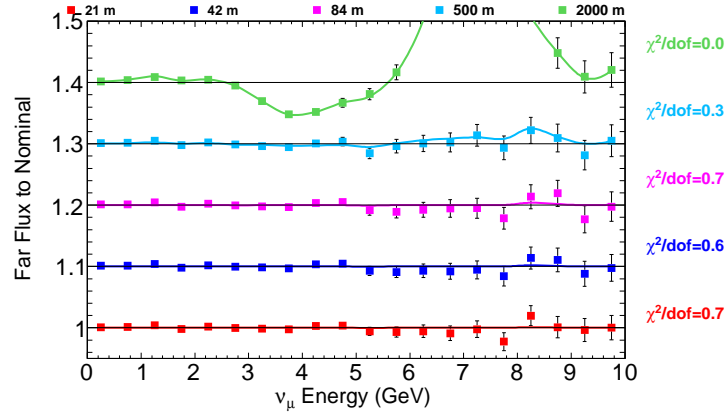


Figure 138: Far detector flux ratio to nominal for several values of **Far detector offset in x** (points) and the results of the fits to each energy bin (lines).

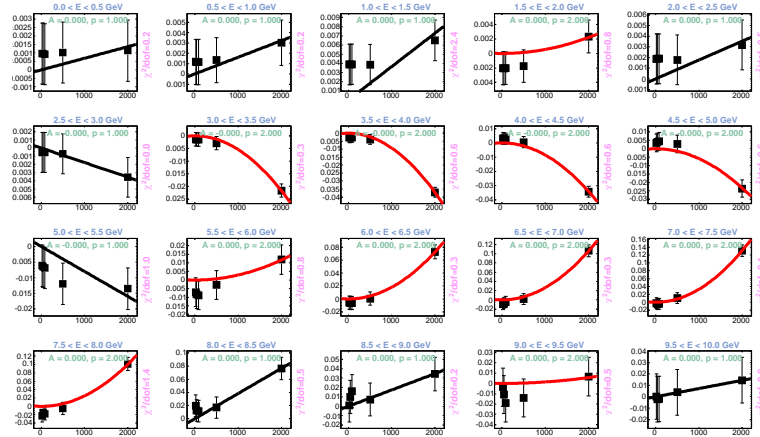


Figure 139: Fits to the far flux ratio for several values of **Far detector offset in x** . Black(Red) fit lines indicate that a linear(parabolic) fit provided the best χ^2 .

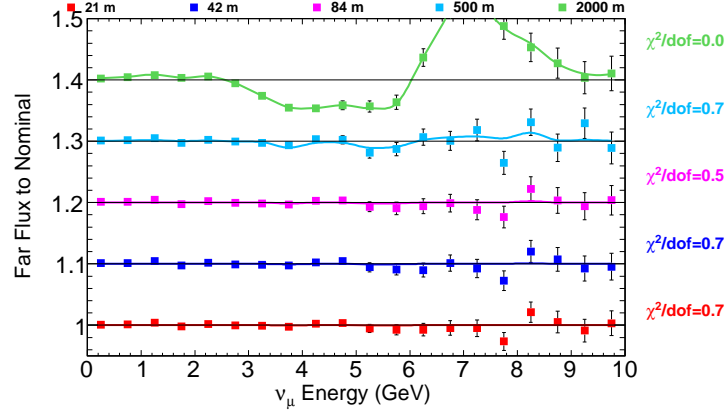


Figure 140: Far detector flux ratio to nominal for several values of **Far detector offset in y** (points) and the results of the fits to each energy bin (lines).

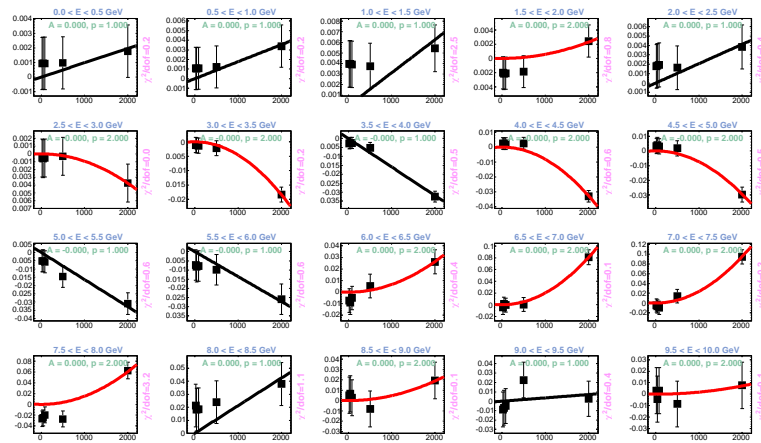


Figure 141: Fits to the far flux ratio for several values of **Far detector offset in y** . Black(Red) fit lines indicate that a linear(parabolic) fit provided the best χ^2 .

C.5 Decay Pipe Position

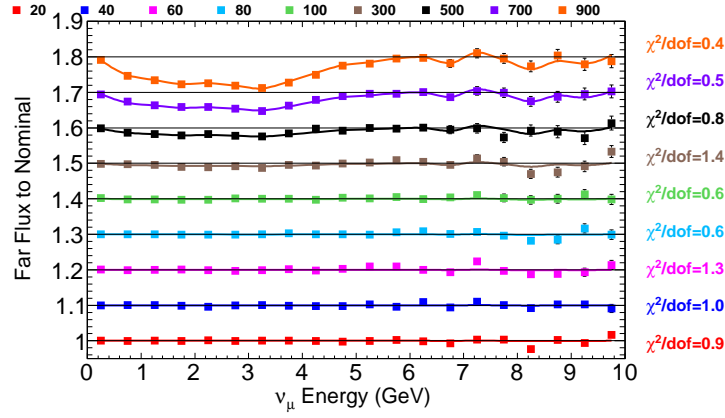


Figure 142: Far detector flux ratio to nominal for several values of **Decay Pipe Offset in x** (points) and the results of the fits to each energy bin (lines).

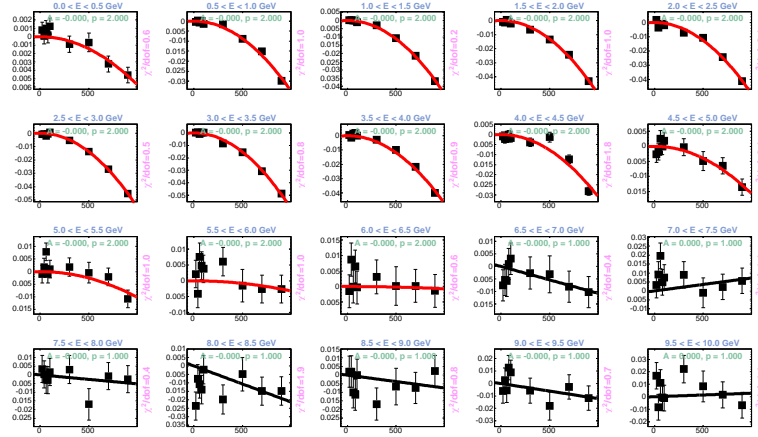


Figure 143: Fits to the far flux ratio for several values of **Decay Pipe Offset in x** . Black(Red) fit lines indicate that a linear(parabolic) fit provided the best χ^2 .

C.6 Decay Pipe Radius

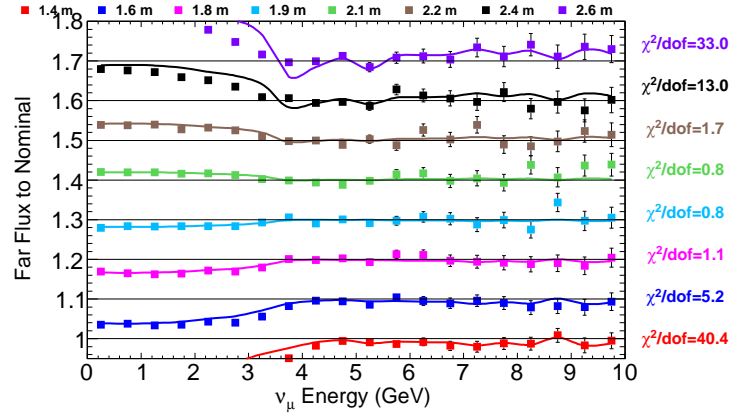


Figure 144: Far detector flux ratio to nominal for several values of **Decay Pipe Radius** (points) and the results of the fits to each energy bin (lines).

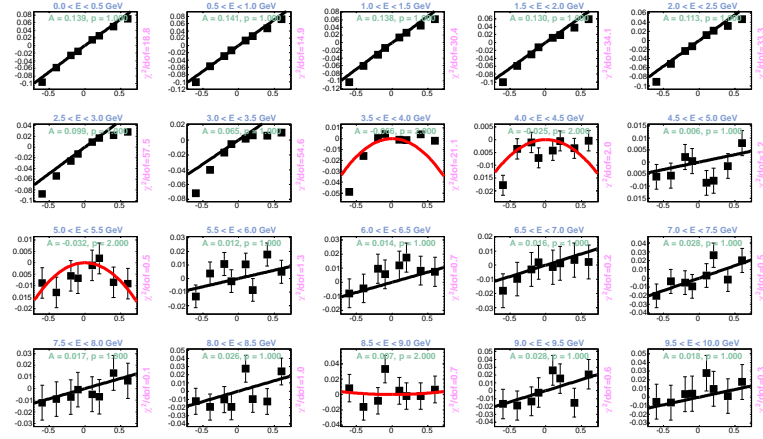


Figure 145: Fits to the far flux ratio for several values of **Decay Pipe Radius**. Black(Red) fit lines indicate that a linear(parabolic) fit provided the best χ^2 .

C.7 Horn Current

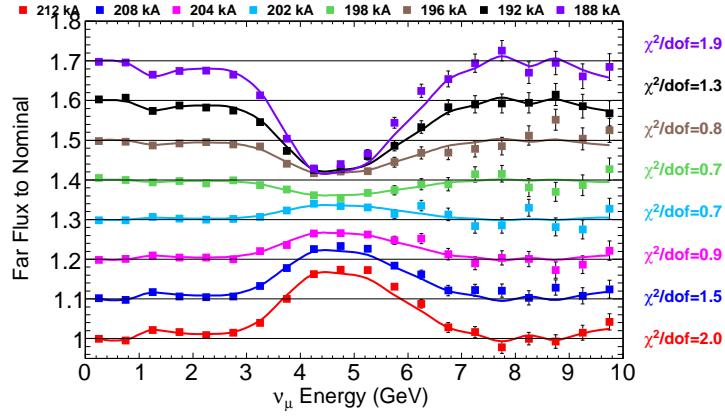


Figure 146: Far detector flux ratio to nominal for several values of **Horn Current** (points) and the results of the fits to each energy bin (lines).

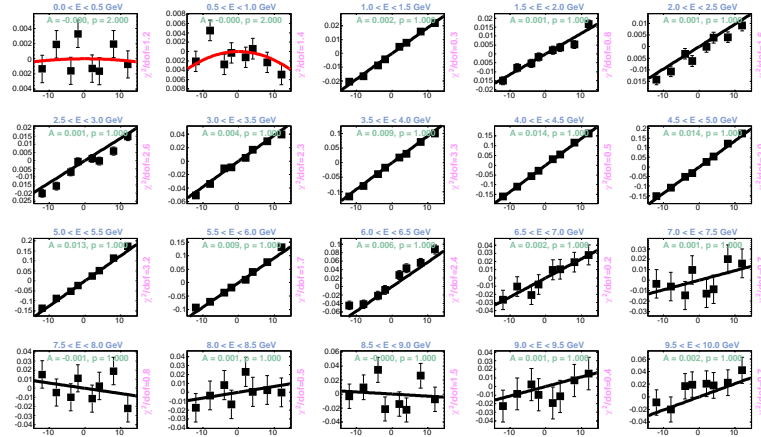


Figure 147: Fits to the far flux ratio for several values of **HornCurrent**. Black(Red) fit lines indicate that a linear(parabolic) fit provided the best χ^2 .

C.8 Horn Water Layer Thickness

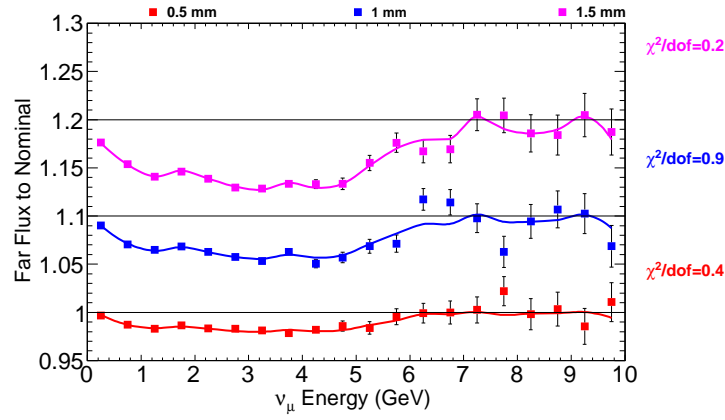


Figure 148: Far detector flux ratio to nominal for several values of **horn cooling water layer thickness** (points) and the results of the fits to each energy bin (lines).

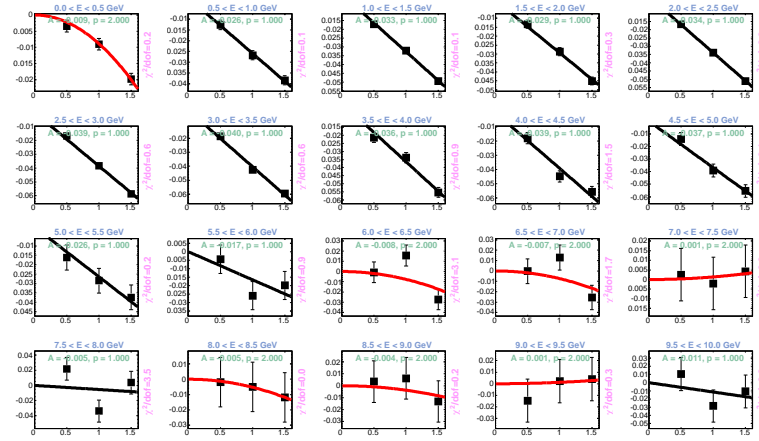


Figure 149: Fits to the far flux ratio for several values of **horn cooling water layer thickness**. Black(Red) fit lines indicate that a linear(parabolic) fit provided the best χ^2 .

C.9 Beam size at target

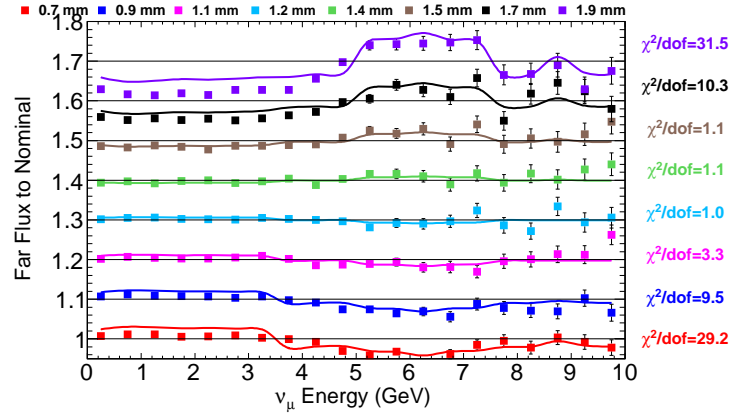


Figure 150: Far detector flux ratio to nominal for several values of **Beam size in x** (points) and the results of the fits to each energy bin (lines).

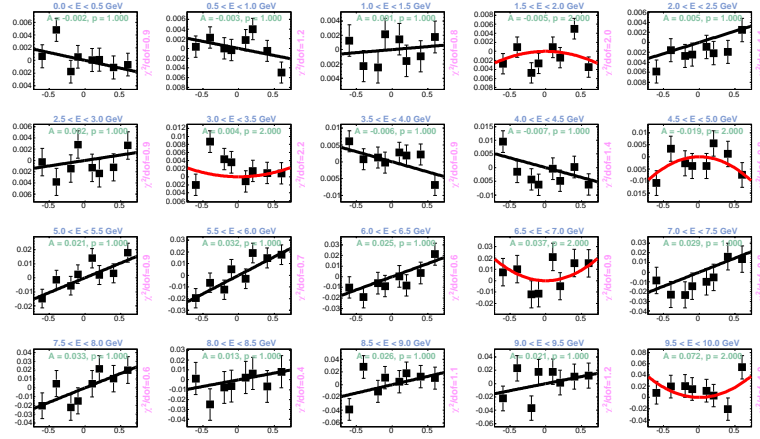


Figure 151: Fits to the far flux ratio for several values of **Beam size in x** . Black(Red) fit lines indicate that a linear(parabolic) fit provided the best χ^2 .

C.10 Beam Position at Target

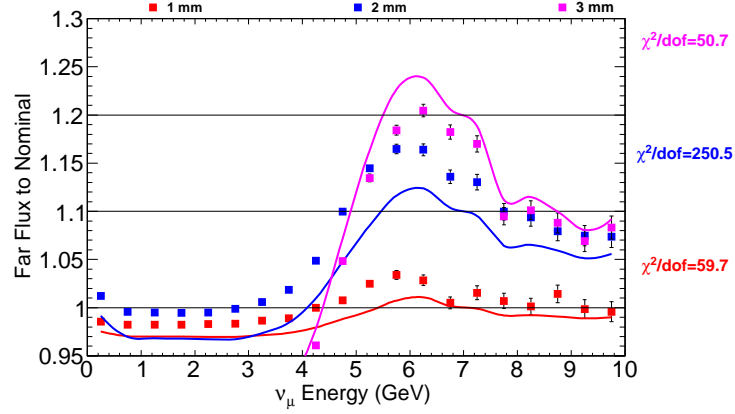


Figure 152: Far detector flux ratio to nominal for several values of **Beam x offset at target** (points) and the results of the fits to each energy bin (lines).

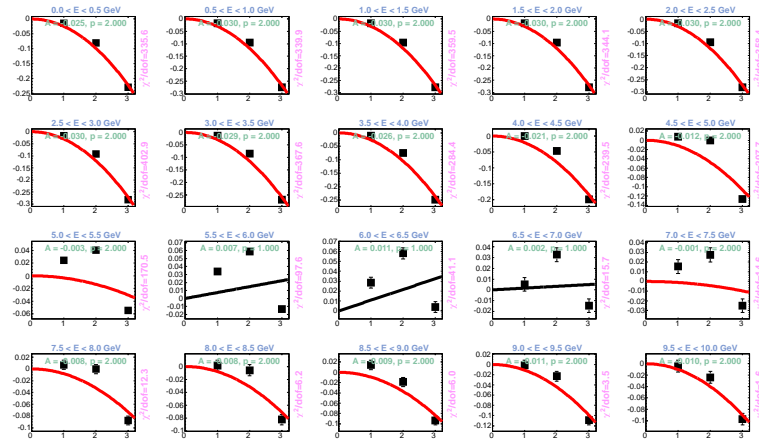


Figure 153: Fits to the far flux ratio for several values of **Beam x offset at target**. Black(Red) fit lines indicate that a linear(parabolic) fit provided the best χ^2 .

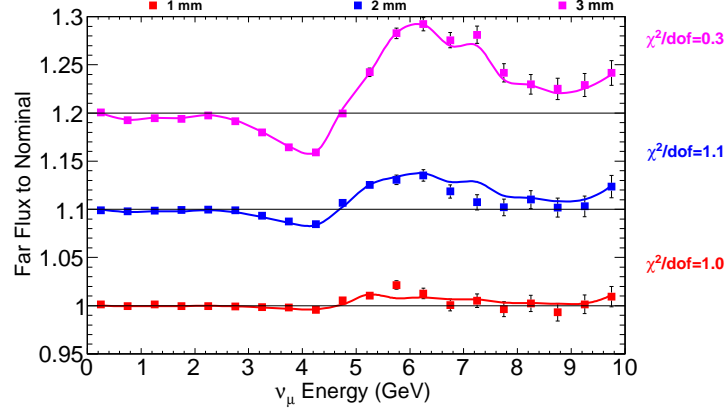


Figure 154: Far detector flux ratio to nominal for several values of **Beam y offset at target** (points) and the results of the fits to each energy bin (lines).

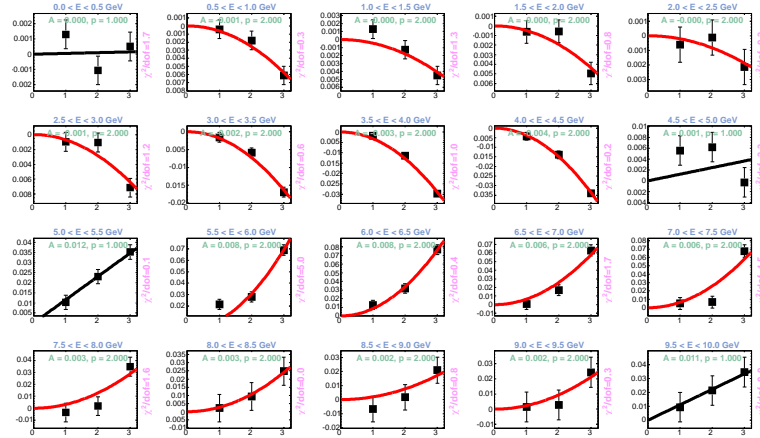


Figure 155: Fits to the far flux ratio for several values of **Beam y offset at target**. Black(Red) fit lines indicate that a linear(parabolic) fit provided the best χ^2 .

C.11 Beam Angle at Target

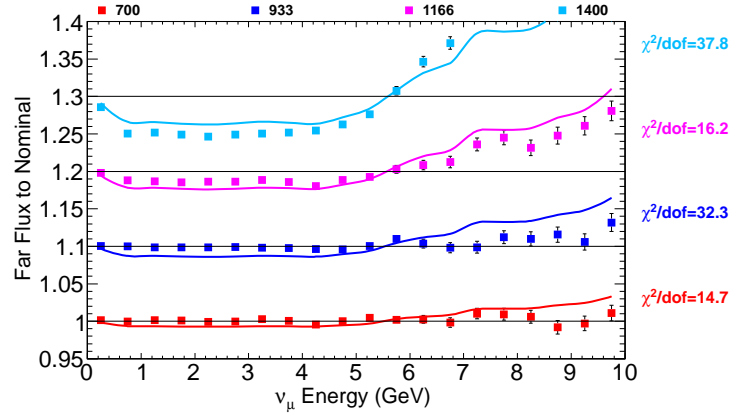


Figure 156: Far detector flux ratio to nominal for several values of **beam tilt in x** (points) and the results of the fits to each energy bin (lines).

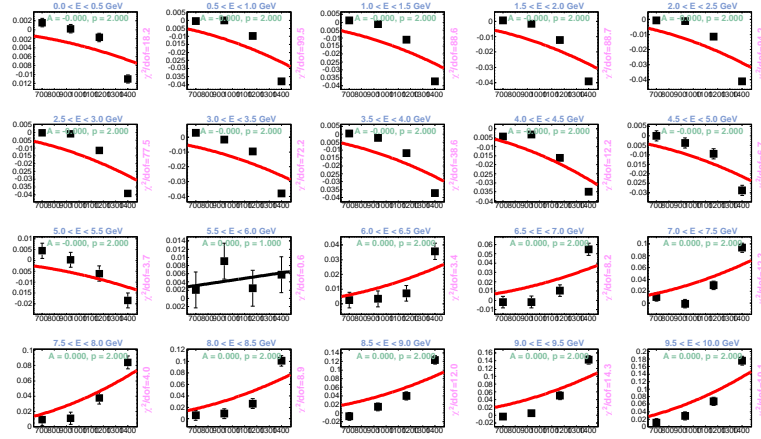


Figure 157: Fits to the far flux ratio for several values of **beam tilt in x** . Black(Red) fit lines indicate that a linear(parabolic) fit provided the best χ^2 .

C.12 Far Detector Position

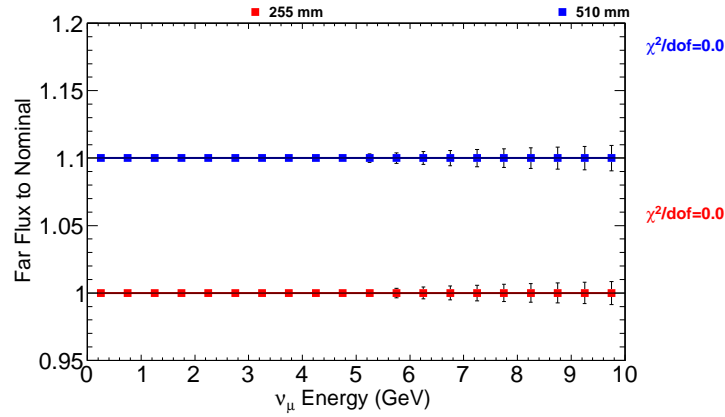


Figure 158: Far detector flux ratio to nominal for several values of **Far detector offset in x** (points) and the results of the fits to each energy bin (lines).

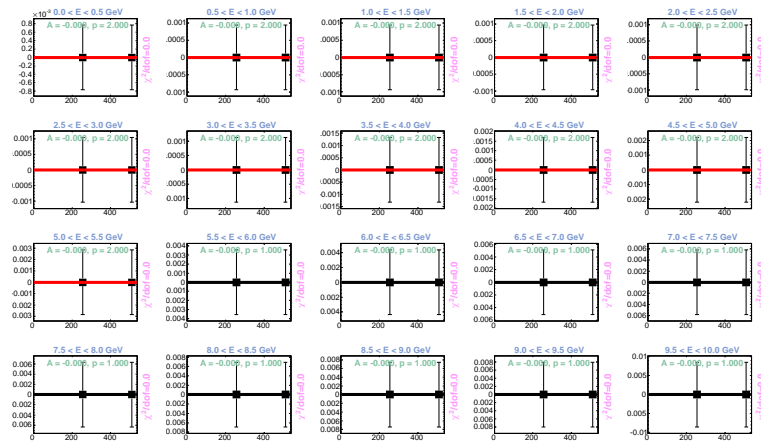


Figure 159: Fits to the far flux ratio for several values of **Far detector offset in x** . Black(Red) fit lines indicate that a linear(parabolic) fit provided the best χ^2 .

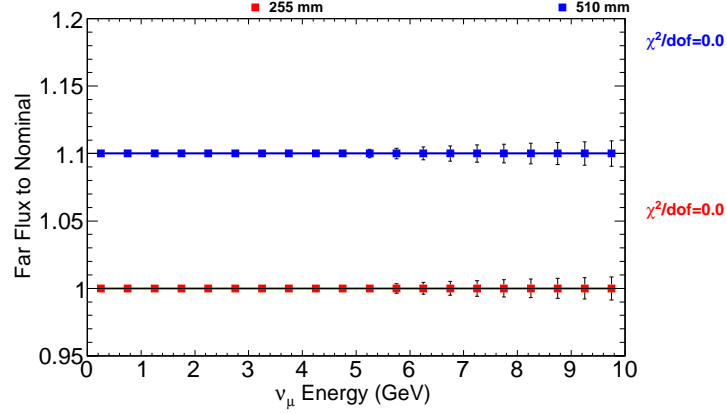


Figure 160: Far detector flux ratio to nominal for several values of **Far detector offset in y** (points) and the results of the fits to each energy bin (lines).

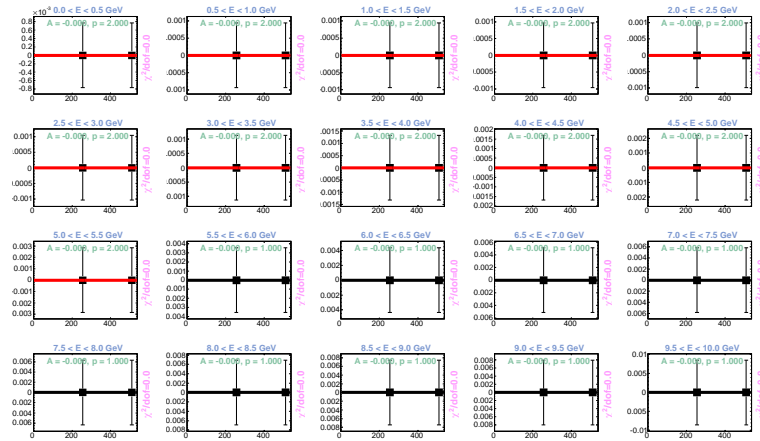


Figure 161: Fits to the far flux ratio for several values of **Far detector offset in y** . Black(Red) fit lines indicate that a linear(parabolic) fit provided the best χ^2 .

C.13 Horn Conductor Skin Depth

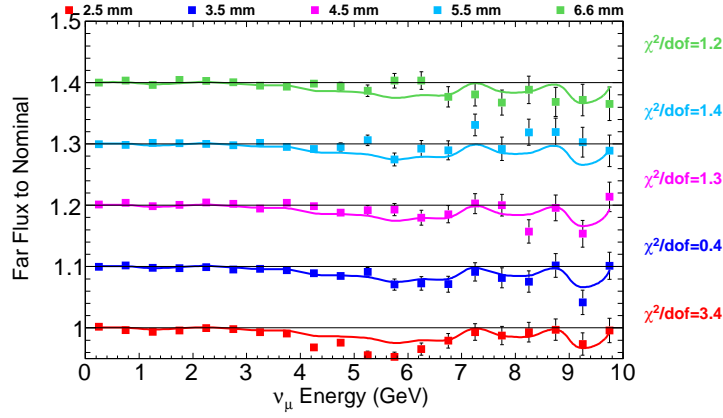


Figure 162: Far detector flux ratio to nominal for several values of **skin depth in the horn conductors** (points) and the results of the fits to each energy bin (lines).

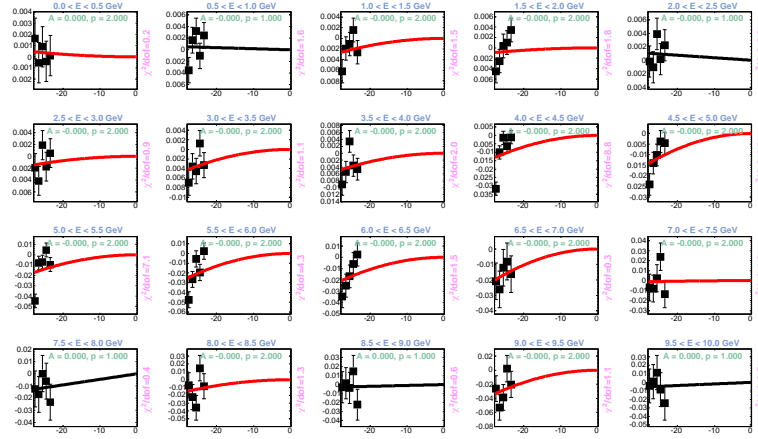


Figure 163: Fits to the far flux ratio for several values of **skin depth in the horn conductors**. Black(Red) fit lines indicate that a linear(parabolic) fit provided the best χ^2 .

References

- [1] LBNE Conceptual Design Report Volume 2: Beamline at the Far Site. LBNE DocDB 4317.
- [2] NuMI Technical Design Handbook, http://www-nuui.fnal.gov/numwork/tdh/tdh_index.html.

- [3] Nuclear Instruments and Methods in Physics Research A 506 (2003) 250-303, and IEEE Transactions on Nuclear Science 53 No. 1 (2006) 270-278.
- [4] <http://www-admscad.fnal.gov/MSDMain/cgi-bin/TPifind-web.pl>